Texas A&M University

Mechanical Engineering Department

Turbomachinery Laboratory

Experimental Response of a Rotor Supported on Flexure Pivot Hydrostatic Pad Gas Bearings

Research Progress Report to the Turbomachinery Research Consortium

by

Luis San Andrés
Professor
Xuehua Zhu
Research Assistant

TRC-B&C-4-03

May 2003

TRC Project:

Experimental Response of Gas Hybrid Bearings for High Speed Oil-Free Turbomachinery

Experimental Response of a Rotor Supported on Flexure Pivot Hydrostatic Pad Gas Bearings

Executive Summary

Micro-turbomachinery demands gas bearings to ensure compactness, lightweight and extreme temperature operation. Gas bearings with large stiffness and damping, and preferably of low cost, will enable successful commercial applications. Presently, tests conducted on a small rotor supported on flexure pivot – hydrostatic pad gas bearings (FPTPBs) demonstrate stable rotordynamic responses up to 99,000 rpm (limit of the drive motor). Experimental rotor responses show the feed pressure increases the bearings' direct stiffness and critical speed while the viscous damping ratio decreases. Predictions correlate favorably with experimentally identified (synchronous) direct stiffness bearing force coefficients. Test gas bearing damping coefficients are 50% or less of the predicted magnitudes, though remaining relatively constant as the rotor speed increases. Tests without feed pressure show the rotor becomes unstable at ~ 81 krpm with a whirl frequency ratio of 20%. The instability caused the rotor to rub and burn its protective Teflon coating. Further tests showed lower threshold speeds of instability due to the enlarged bearing clearances.

The dynamic performance of the FPTPBs is superior to that of simple hydrostatic three-lobed bearings (tested in 2002), which showed severe subsynchronous instabilities, and whose threshold speed increased with feed pressure.

FPTPBs are mechanically complex and more expensive than cylindrical plain bearings. However, their enhanced stability characteristics and predictable rotordynamic performance makes them desirable for the envisioned oil-free applications in high speed micro turbomachinery.

Acknowledgments

Thanks to former student Deborah Wilde for designing the test bearings and to KMC, Inc., for manufacturing the bearings to the desired specifications. The assistance of graduate student Gautam Gupta is also recognized.

TABLE OF CONTENTS

LIST OF TABLES

LIST OF FIGURES

NOMENCLATURE

A	Effective orifice area [m^2]
C	Bearing radial clearance [m]
C_p	Pad clearance [m]
C_{ij}	Bearing damping coefficients; $i, j = X, Y$ [N-s/m]
d_o	Feed orifice diameter [m]
D	Nominal rotor diameter [m]
D_b	Bearing bore diameter [m]
D_f	Rotor diameter after coating [m]
e_X, e_Y	Journal eccentricity components [m]
F_X, F_Y	Transmitted (synchronous sped) bearing forces [N]
k	Air adiabatic constant
K_{ij}	Bearing stiffness coefficients; $i, j = X, Y$ [N/m]
K_{eq}	Bearing equivalent stiffness coefficient [N/m]
L_r	Rotor length
L	Bearing axial length [mm]
m_i	Calibrated imbalance mass [g]
$\dot{m}$	Bearing mass flow rate [kg/s]
M	Rotor mass [kg]
M_1	Half of rotor mass [kg]
N_n	Rotor speed at natural frequency [rpm]
N_1, N_2	Speeds corresponding to 70% peak displacement at N_n [rpm]
P	Film pressure [bar]
P_s	Supply pressure [bar]
P_o	Orifice discharge pressure [bar]
P_a	Ambient pressure [bar]
r	Bearing preload [-]
R	Rotor radius [m]
R'	Radial location of imbalance mass [m]
$\mathfrak{R}$	Air constant [J/kg-K]
T	Air temperature [K]
ρ_A	Air density at ambient pressure [kg/m^3]
u	Imbalance displacement [m]
U_1, U_2, U_1', U_2'	Calibrated imbalance displacements [m]
X, Y, z	Inertial coordinate system
ω_c	Rotor critical speed [rad/s]
Ω,, ω	Rotor rotational speed and excitation frequency [rad/s]
ζ	Damping ratio at critical speed [-]
θ	Circumferential coordinate [rad]
μ	Gas viscosity [Pa-s]

Introduction

Gas film bearings, unlike oil-lubricated bearings, offer advantages of low friction and less heat generation. These advantages enable their successful applications in air-cycle units for airplanes, high-precision instruments, auxiliary power units, and high-speed micro-turbomachinery. In addition, gas bearing systems do not require costly, complex sealing and lubricant circulation systems. Furthermore, these oil-free bearing applications eliminate process fluid contamination and are environmental friendly.

The main disadvantages of gas film bearings are little damping and low load capacity because of the gas inherently low viscosity. The provision of pressurized gas during start-up and shutdown periods is mandatory to overcome transient rubs between metal surfaces. A hybrid bearing configuration offers the combination of hydrostatic and hydrodynamic effects on the bearing static and dynamic forced performance. Incidentally, infamous disadvantages stem from two major kinds of instability [1]. One is pneumatic hammer controlled by the flow versus pressure lag in the pressurized gas feeding system. The other is a hydrodynamic instability, a self-excited motion characterized by subsynchronous (forward) whirl motions. A properly designed hybrid bearing system aids to minimize these two kinds of instabilities.

Wilde and San Andrés [2] describe comprehensive rotordynamic experiments conducted on a small rotor supported on three lobed hybrid gas bearings. These bearings are simple and inexpensive with static and dynamic force characteristics desirable in high-speed turbomachinery. These characteristics are adequate load support, stiffness and damping coefficients, low friction and wear during rotor startup and shutdown, and most importantly, enhanced rotordynamic stability. The rigid bearings comprise of preloaded 120° lobes with minute feed holes for external pressurization. The test rotor, weighing 827 grams, integrates a DC motor and can achieve speeds to 100,000 rpm. For various imbalance conditions, coast down tests from 60,000 rpm characterize the rotor response supported on the bearings. As the supply pressure rises, the rotor response shows an increase in critical speed and a noticeable reduction in damping ratio. Threshold speeds of instability also increase with increasing supply pressures, and whirl frequency ratios range from nearly 50% of rotor speed for a purely hydrodynamic condition to 25 % for a pressure supply five times ambient.

The current investigation focuses on flexure pivot – tilting pad gas bearings (FPTPBs). This bearing type is a one-piece mechanical component fabricated with the electric discharge machining (EDM) process. Each pad connects to the bearing through a thin flexural web, which provides a low rotational stiffness, thus ensuring small cross-coupled stiffness coefficients and avoiding subsynchronous instabilities into very high speed operation [3]. FPTPBs also eliminate tolerance stack-up during manufacturing and assembly, as reduce pad wear and pivot contact stresses.

The objective of the current work is to investigate experimentally the dynamic forced performance of a rotor supported on gas FPTPBs supplied with pressurized air, i.e. a hybrid bearing configuration. Rotor dynamic displacements and bearing transmitted forces are measured during coast-down tests to baseline and calibrated imbalance masses. Run-up tests are conducted to high speeds in search of regions of rotordynamic unstable response regions. The bearings stiffness and damping coefficients are estimated from the measured responses. Predicted stiffness and damping coefficients are in close agreement with the identified bearing coefficients.

Literature Review

Gas lubricated bearings have attracted considerable attention since half a century ago. Their unique advantage of reduced power losses is well known. During its initial development, gas bearings were limited to aerospace turbo expanders, navigation systems and instrumentation tools [4, 5], where oil lubricated bearings could not be used due to high speed or extreme temperature concerns. Gas bearings also eliminate bulky lube oil systems and sealing elements, thus allowing for compact rotor-bearing systems with less number of parts. Gas bearings, however, have a very low load carrying capacity and require of minute film thickness to accomplish their intended function. Thus, their fabrication and installation tends to be expensive and time consuming. In addition, rigid geometry gas bearings offer little damping due to the low viscosity of the process gas used, and thus are not able to limit rotor motions while traversing critical speeds. Furthermore, rigid gas bearings are prone to show self-excited instabilities limiting their application to rotor speeds not exceeding twice the first natural frequency of the rotor-bearing system [6].

Tilting pad gas bearings eliminate the infamous hydrodynamic instability by not generating cross-coupled stiffness coefficients. However, this type of bearing is mechanically complex and each pad has several degrees of freedom, including pitch, yaw and roll. Thus, comprehensive analyses are necessary to determine the adequate bearing geometry. Elwell and Findlay [7] detail a design method and present charts for bearing performance characteristics as a function of the slenderness (L/D) ratio, number of pads, clearance, pivot location, load direction, etc. Although instabilities are less severe in a tilting-pad bearing than in most other types of bearings, they nevertheless exist. The multiplicity of parameters associated with a tilting pad bearing demands complex analytical methods for force coefficients and stability predictions. Lund [8, 9] provides a perturbation solution of the Reynolds equation to obtain frequency dependent, linearized dynamic force coefficients of a tilting pad bearing, and investigates the influence of pad flexibility on the dynamic force coefficients.

Tilting pad bearings support critical turbomachinery operating well above critical speeds and are not prone to induce subsynchronous instabilities. However, their time-accumulating drawbacks, namely pad wear and flutter and loss of nominal clearance, result in poor performance in the long run. The flexure pivot – tilting pad bearing (FPTPB) offers a marked improvement over the conventional design since its wire EDM construction renders an integral pads-bearing, thus eliminating pivot wear and stack up of tolerances on assembly. Chen et al [10] describe the EDM process to fabricate FPTPBs.

The rotational structural stiffness of the pad web determines the amount of cross-coupled stiffness coefficients in a FPTPB [2]. A large rotational stiffness (thick web) makes the FPTPB work as a rigid pad bearing with its inherent instability problem. Low rotational web stiffnesses make an ideal tilting pad bearing; however, concentrated web stresses and fatigue may be of concern [11]. Nonetheless, proper engineering design can lead to a substantial margin of the endurance limit for the web structural material.

Armentrout et al [11] show that large pad clearances aid to improve the stability of FPTPBs. Chen et al. [10] also demonstrate that offset pivot designs provide higher stiffnesses, reduce the bearing sensitivity to clearance changes, and offer a higher logarithmic decrement. Successful applications [12, 13] demonstrate FPTPBs have a larger load capacity and lower lubricant temperature raise than conventional tilting pad bearings.

The provision of pressurized gas during start-up and shutdown periods is mandatory to overcome transient rubs between metal surfaces. In addition hydrostatic effects provide supplemental stiffness for operation at all rotational speeds and reduce the operating rotor eccentricity. Thus, a hybrid mode operation ultimately results in reduced power consumption.

References [14-16] advance the first analyses for prediction of gas bearing static and dynamic forced performance. Two kinds of (self-excited) instabilities are apparent in hybrid gas bearings, i.e. pneumatic hammer and hydrodynamic. The first one is due to gas trapped in local volumes and whose pressure is out of phase with the rotor motion [17]. Improper restrictor design with large volumes leads easily to this dangerous instability that can occur even without rotor spinning. Hydrodynamic instability is due to the sudden loss of effective damping at whirl frequencies at typically 50% of rotor speed and coinciding with a system natural frequency. San Andrés and Childs [18] demonstrate that hybrid bearings with angled injection improve rotordynamic performance with virtual elimination of cross-coupled stiffness coefficients and null or negative whirl frequency ratios. Lee et al. [19] propose an active control method to improve the stability characteristics of externally pressurized air journal bearings.

Czolczynsk [20] provides a comprehensive review of gas bearing applications and the numerical analysis for prediction of frequency dependent force coefficients. San Andrés and Wilde [20] advance the finite element analysis of gas bearings with numerically accurate results into very high speed numbers. References [2], [22] and [23] detail the research at TAMU on inexpensive gas bearings.

The present work advances the technology of gas film bearings, FPTPB type, for applications to oil-free turbomachinery by demonstrating their rotordynamic performance, reliability and durability.

Experimental Facility

Figure 1 shows the experimental high speed test apparatus and instrumentation for gas bearing investigations. Wilde [23] evaluated the dynamic forced performance of three-lobed, pressure dam and tilting pad gas bearings with this test rig.

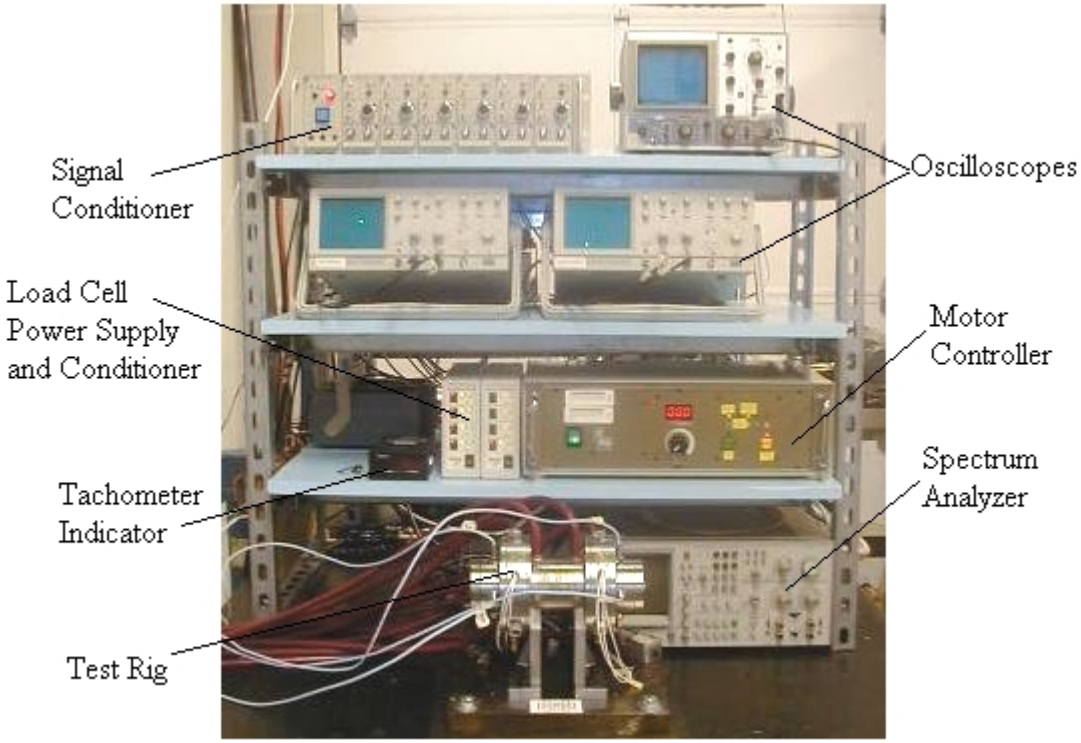

Figure 1 Gas bearing test rig and instrumentation

Figure 2 depicts the test rig of symmetric construction and with a steel main body integrating a brushless DC motor armature. The motor controller provides 0.9 kW of continuous power and is protected by 1.0 amp fuses. The maximum continuous speed can approach 99,000 rpm. A K-type thermocouple attached to the motor inside the test chamber monitors the temperature of the motor armature. A rapid temperature rise is a good indicator of solid surface contact of the rotor with its bearings.

The motor drives a rotor supported by two identical flexure pivot pad gas bearings. This rotor, shown in Figure 3, consists of a steel shaft, 15mm diameter and 190mm in length, onto which two cylindrical sleeves are press-fit. The rotor has an original diameter of 28.48±0.001 mm. A coating of Permalon® enlarged the rotor diameter to 28.52±0.003 mm at the bearing locations. The Teflon coating is applied as a spray at room temperature. Eight 1 mm in diameter holes are spaced equally at each rotor end face. Imbalance masses can be placed in these holes for imbalance response measurements. Thrust pins in both casing covers prevent axial rotor movements.

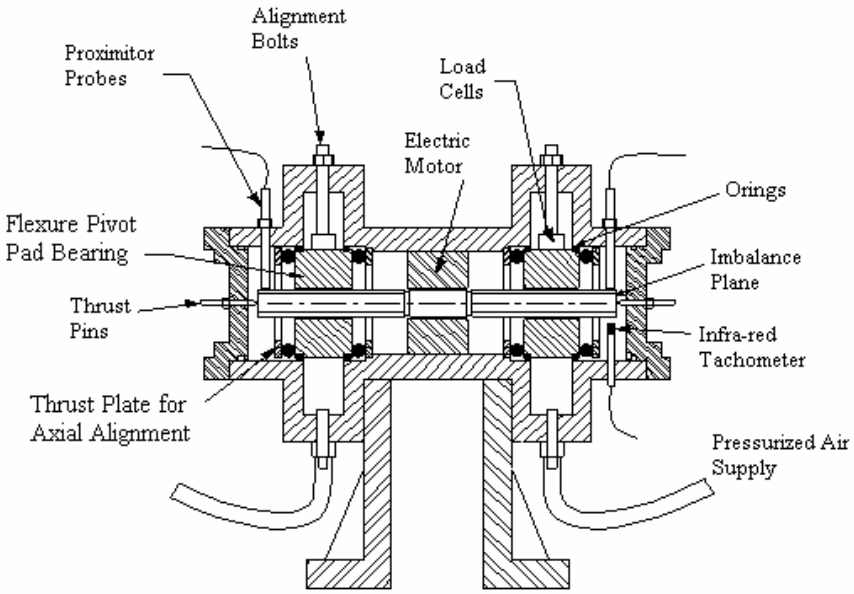

Figure 2 Schematic cross section view of test rig

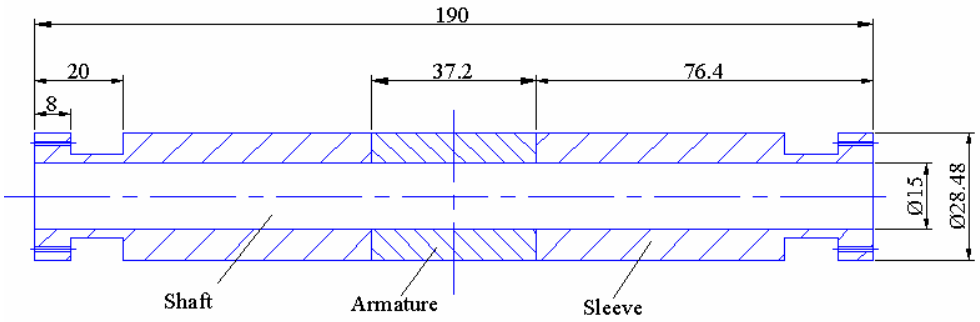

Figure 3 Schematic view of rotor with shaft, motor armature and press-fit sleeves (units: mm)

Figure 4 depicts the design drawing and picture of the test flexure pivot gas bearings. Each bearing has 4 arcuate pads with 60% pad pivot offset. The nominal bearing bore diameter is 28.56 ± 0.003 mm with a 40% machined preload[1]. Pressurized air can enter the bearing through eight identical orifices in the middle plane of the bearing. Four radial holes are machined directly through the flexural webs and serve to pressurize directly each pad. The other four holes (not radial due to construction difficulties) discharge in the regions between adjacent pads. In the experiments, these last feed holes are plugged. The bearings are installed in the (static) load between pads configuration. Table 1 lists the main dimensions of the test rotor and the hybrid FPTPBs.

[1] Preload (r) is a function of the shaft diameter, bearing diameter and pad diameter and defined as $r = \frac{C_p}{C}$.

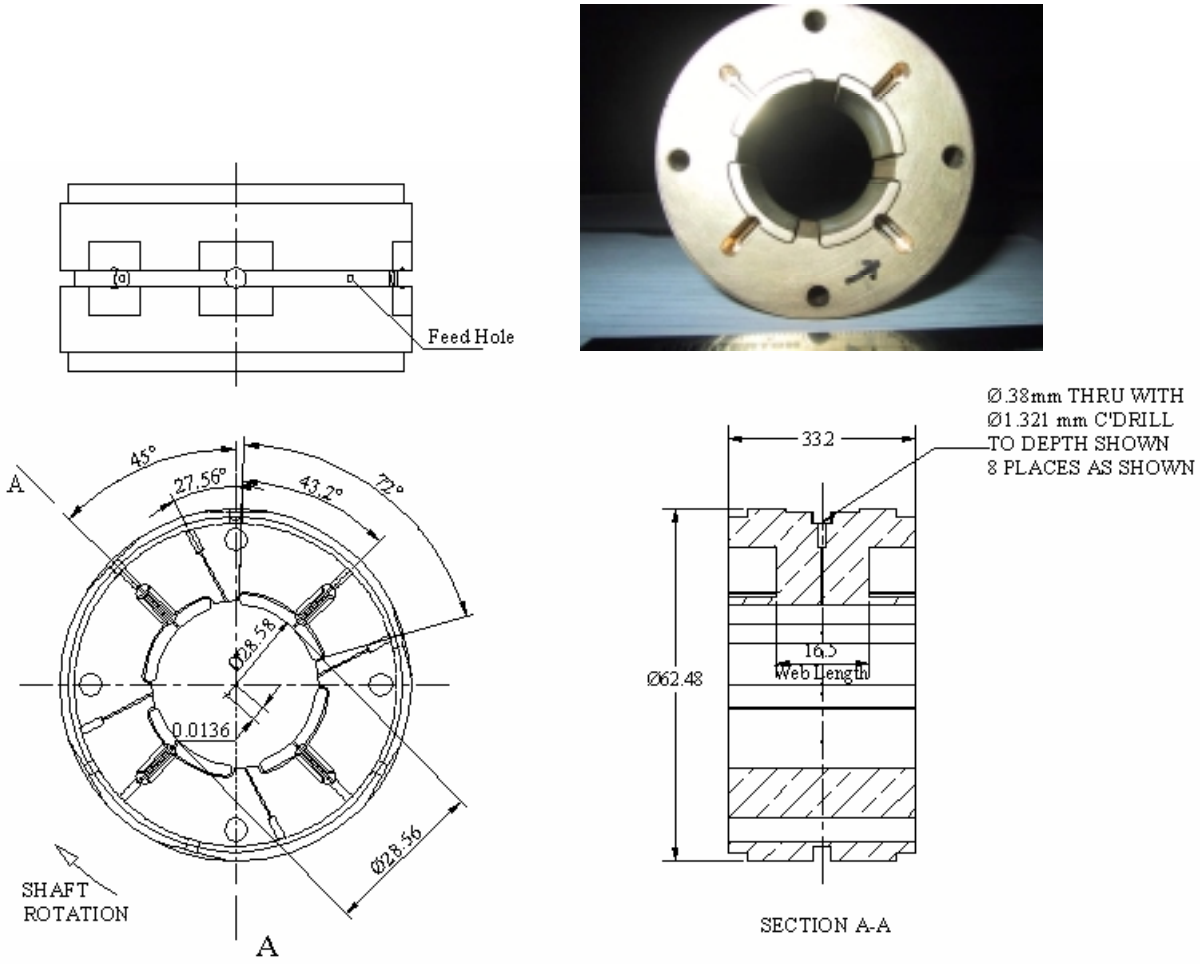

Figure 4 Flexure pivot hydrostatic pad gas bearing. Photograph of bearing and details of bearing geometry

Table 1 Main parameters of test rig and flexure pivot bearings

Parameter	*Value*	*Unit*
Rotor Mass, *M*	0.827	kg
Rotor Diameter, *D*	28.48 ± 0.001	mm
Rotor Length, L_r	190	mm
Final Rotor Diameter with coating, D_f	28.52 ± 0.003	mm
Bearing Bore Diameter, D_b	28.56 ± 0.003	mm
Bearing Diametrical Clearance, *2C*	40 ± 4.5	μm
Radial Preload Clearance, C_p	8	μm
Bearing Axial Length, *L*	33.2	mm
Pivot offset	60%	N/A
Bearing dimensionless preload, *r*	40%	N/A
Pad Number	4	N/A
Pad Arc	72	Degrees
Number of feed orifices	8	N/A
Nominal diameter for each feed orifice	0.38	mm

The bearings are installed into the test rig with load cells and positioned using three alignment bolts 120 ° apart. A cover plate pushes each bearing into the test rig, and O-rings on each bearing side seal the bearing chamber preventing air leakage. Alignment plates and loose through bolts assist in the positioning of each bearing within its housing. The airflow into the bearing is controlled by on/off valves connected to the main pressure source (shop line). The gas piping system includes a pressure regulator, dryer/filter, and pressure gauges and flowmeters.

Figure 2 shows two orthogonally positioned eddy-current displacement transducers installed into each casing end to measure rotor motions. These transducers recording voltages are connected to a signal conditioner to remove the large DC bias offset and convert the signals within suitable ranges for the Labview® data acquisition system. Each oscilloscope displays the real-time, unfiltered shaft orbit at the end side monitored. Unconditioned signals from the eddy-current transducers are connected to a Bently Nevada ADRE® data acquisition system. A two-channel dynamic signal analyzer displays the frequency components of selected signals in real time.

Three piezoelectric load cells, 120° apart, are mounted at the center plane of each bearing. The force sensors measure the load transmitted through the bearings. Three alignment bolts preload the load sensors and aid in the positioning of each bearing. Figure 5 shows a picture of the assembly. An infrared tachometer, shown in Figure 2, installed inside one of the bearing chambers records the rotor speed and offers a keyphasor signal for data acquisition. Table 2 provides the sensitivities of the displacement and load sensors and the range of the flowmeters.

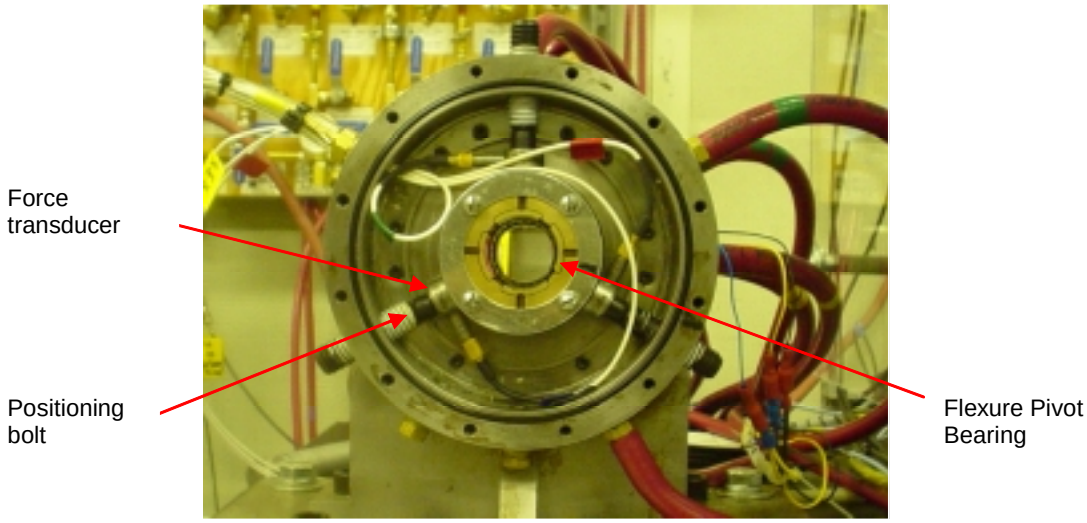

Figure 5 View of test rig bearing chamber including force transducers and positioning bolts

Table 2 Sensitivities and ranges of sensors

Name	Location	Sensitivity	Unit
Force Transducer	Left Bearing	119	mV/N
	Right Bearing	120	mV/N
Displacement Proximity probe	Left Bearing	40	mV/μm
	Right Bearing	40	mV/μm
Flow Meter (range)	Left Bearing	100	L/min
	Right Bearing	50	L/min

A Bentley Nevada ADRE® data acquisition system acquires and saves the data during rotor coast-down response tests. The ADRE® DAQ system has two channels for keyphasor signals and eight input channels for other signals. Four rotor displacement signals and a maximum of four load sensor signals can be collected simultaneously. The ADRE® system provides various outputs including Bode plots, cascade diagrams, orbit plots, spectrum diagrams, real time slow roll subtraction as well as synchronous response filtering. The maximum rotor speed for the ADRE® system is 60,000 rpm. A Labview® DAQ system is available to provide snapshot views of the experiment and as a supplement tool for high speed tests above 60,000 rpm.

Experimental Procedure

Coast-down speed tests record the rotor dynamic motions and transmitted bearing loads for various imbalance conditions and three feed absolute pressures, 2.39, 3.77 and 5.15 bars (20, 40 and 60 psig). Pressurized air enters into each bearing pad through the small feed orifices in the webs. The holes between adjacent pads are plugged. Appendix A shows the measured bearing mass flow rates and the estimation of the orifice discharge coefficient. This empirical coefficient is of importance for analytical predictions of the bearings performance.

The imbalance measurements consist of a baseline (remnant imbalance) response and calibrated mass imbalance responses. Known added masses determine two imbalance conditions, namely one exciting the rotor cylindrical mode motion and the other one for rotor conical mode motions. The added masses (m_i) are placed in holes at each rotor end at a radial location (R') of 12 mm. The imbalance displacement (u), i.e. distance from rotor center of mass, is

$$u = \frac{m_i R'}{m_i + M_l} \tag{1}$$

where M_l is half the rotor mass (0.4135 kg).

Figures 6 and 7 depict the imbalance mass locations on each rotor end for excitations of the cylindrical and conical modes of vibration, respectively. Table 3 summarizes the imbalance configurations for both tests.

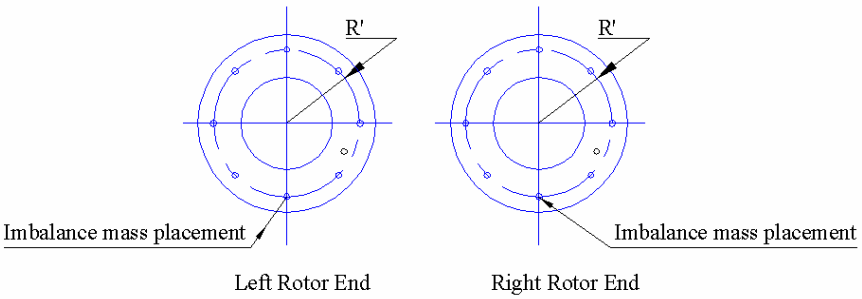

Figure 6 Imbalance mass location at rotor ends for cylindrical mode excitation

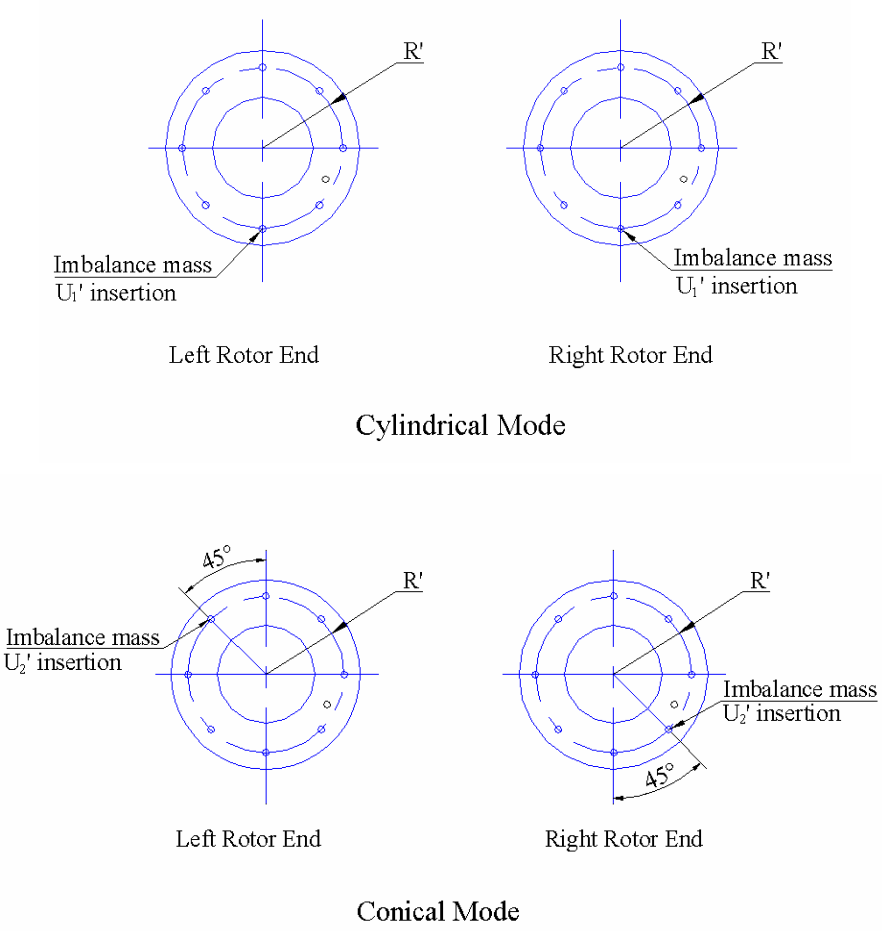

Figure 7 Imbalance mass location at rotor ends for cylindrical and conical mode excitation

Table 3 Mass imbalances for cylindrical and conical mode motions

Cylindrical mode

Imbalance Name	Mass m_i (gram)	Displacement u (μm)
Remnant	N/A	N/A
U1	0.046 ± 0.0008	1.335 ± 0.023
U2	0.054 ± 0.0008	1.567 ± 0.023

Conical mode

Imbalance Name	Mass m_i (gram)	Displacement u (μm)	Imbalance Mode
U1’	0.050 ± 0.0008	1.451 ± 0.023	Cylindrical
U2’	0.050 ± 0.0008	1.451 ± 0.023	Conical

Experimental Results

Baseline Responses

Figure 8 depicts the peak-peak direct synchronous rotor displacement amplitudes due to its remnant imbalance versus rotor speed. The test corresponds to a feed absolute pressure of 3.77 bars (40 psig). In the Bode plot, the designations LH and LV correspond to the displacements at the left bearing end, horizontal and vertical, respectively. A similar notation follows for the right bearing end, RH and RV. The rotor motion contains mainly synchronous frequency without traces of subsynchronous activity to 60,000 rpm. Note that the rotor motions have large run-out amplitudes, evident at the lowest rotor speeds. These slow roll motions, amplitude and phase, are vector subtracted to better evidence the rotor synchronous response.

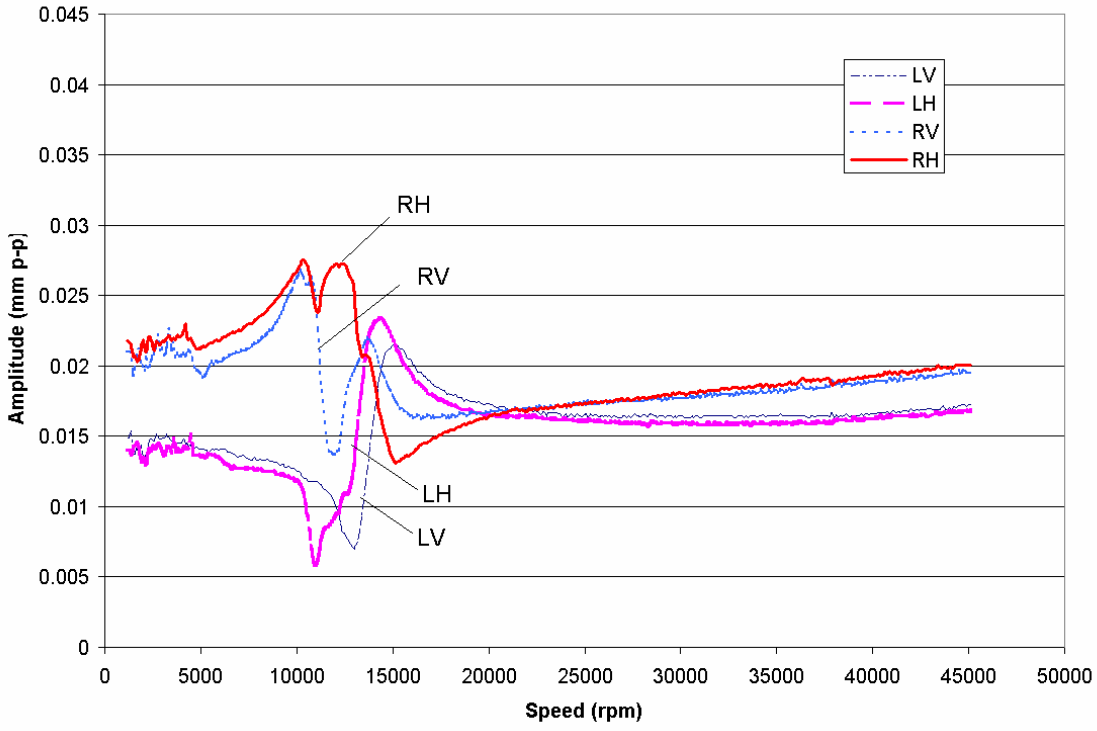

Figure 8 Baseline direct rotor (synchronous) peak-peak amplitudes for test at 3.77 bar absolute feed pressure

Figure 9 depicts the rotor baseline synchronous displacement response with sow roll compensation at 2095 rpm. Two critical speeds are evident and due to the stiffness asymmetry in the vertical and horizontal directions. The largest peak-peak amplitudes of motion, nearly 0.020 mm, occur while passing a cylindrical mode critical speed. Rotor operation shows decreasing amplitudes of motion above the critical speed.

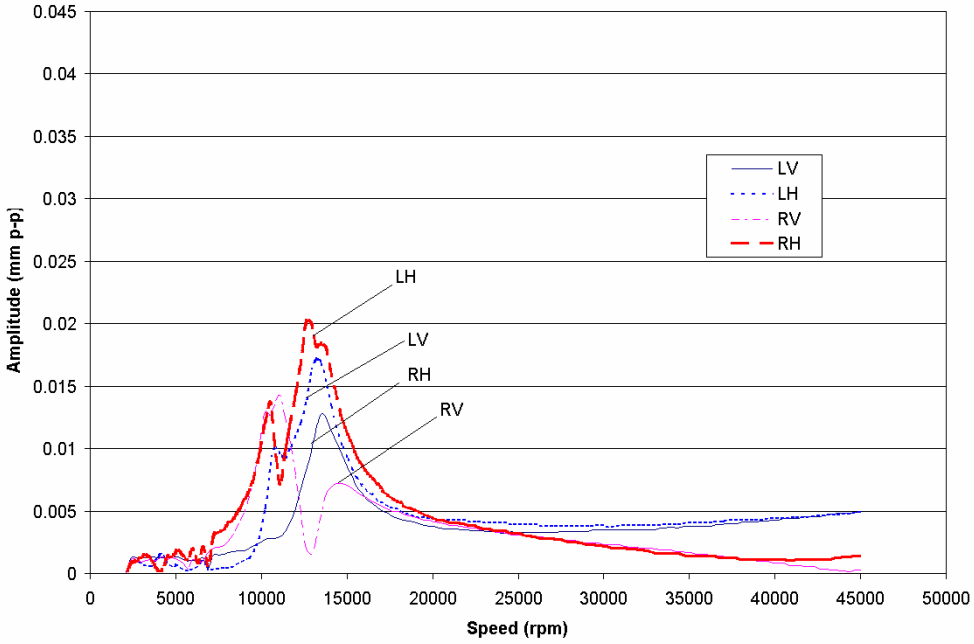

Figure 9 Baseline synchronous rotor peak-peak amplitudes for test at 3.77 bar absolute feed pressure. Slow roll compensation at 2095 rpm

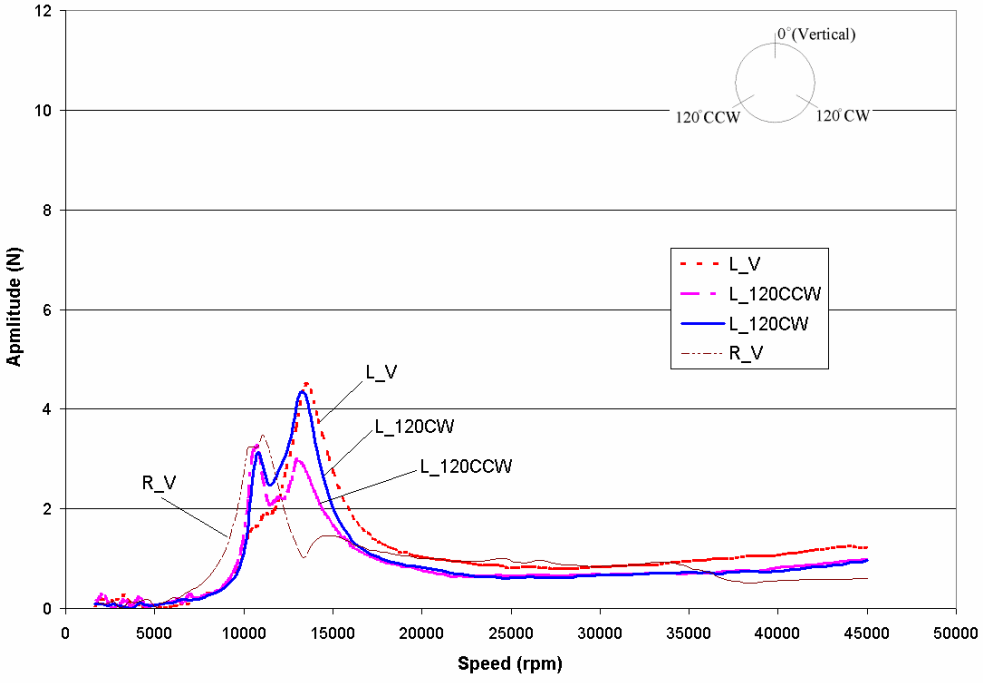

Figure 10 Transmitted bearing force amplitude from baseline synchronous response, 3.77 bar absolute feed pressure. Left bearing load sensors (three orientations), right bearing (vertical)

Figure 10 shows the bearing transmitted forces from the baseline rotor response. The notations in the figure indicate the force transducer locations; namely, L_V for left bearing vertical direction; L_120CCW and L_120CW for the same bearing load sensors positioned 120 degree away from the vertical plane, counter and clockwise, respectively; and R_V for the load along the vertical plane in the right bearing. The transmitted bearing force amplitudes show similar behavior as the rotor displacements, and with amplitudes ranging from 3 N to 4.5 N at the critical speeds. The bearing transmitted loads are nearly negligible in the high-speed range, 20,000 rpm to 45,000 rpm.

Figure 11 display a waterfall plot for the baseline rotor response for speeds to nearly 60 krpm. The response corresponds to a feed pressure of 3.77 bars (40 psig). Note the absence of subsynchronous instabilities. The frequency content of the displacement response is mostly synchronous, albeit some small amplitude motions at twice rotor speed are evident.

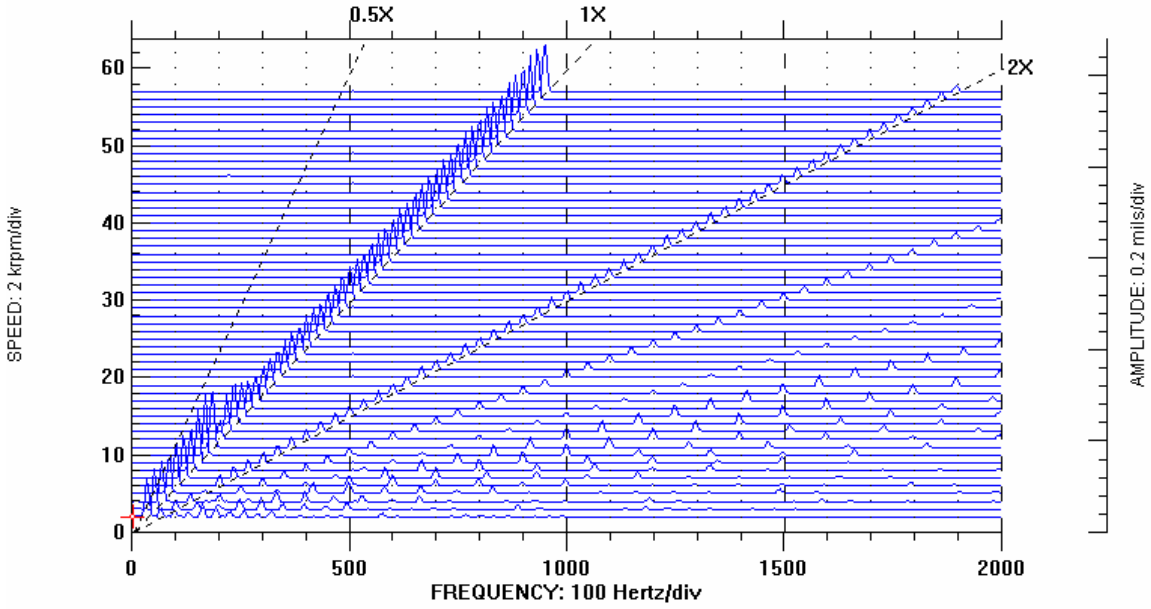

Figure 11 Waterfall plot of rotor amplitudes from baseline synchronous response. Right bearing vertical plane (RV). Test at 3.77 bar absolute supply pressure

Figure 12 depicts the slow-roll compensated synchronous rotor amplitudes for three feed pressures. The supply pressures are 2.39, 3.77 and 5.15 absolute bars, corresponding to 20, 40 and 60 psig, respectively. The critical speeds for each feed pressure condition are 11,400 rpm, 13,500 rpm, and 15,300 rpm. Note that the rotor motion amplitudes increase with feed pressure while traversing a critical speed. Thus, as previously shown in [2, 22], hydrostatic pressurization increases the gas bearing direct stiffness and lowers the system damping ratio while traversing a critical speed.

Figure 13 displays the transmitted (left vertical) bearing loads versus rotor speed for increasing feed pressures. Note the rapid increase in transmitted load as the feed pressure

increases. The largest magnitude of about 6 N is nearly 50% higher than half the rotor weight (4.05N).

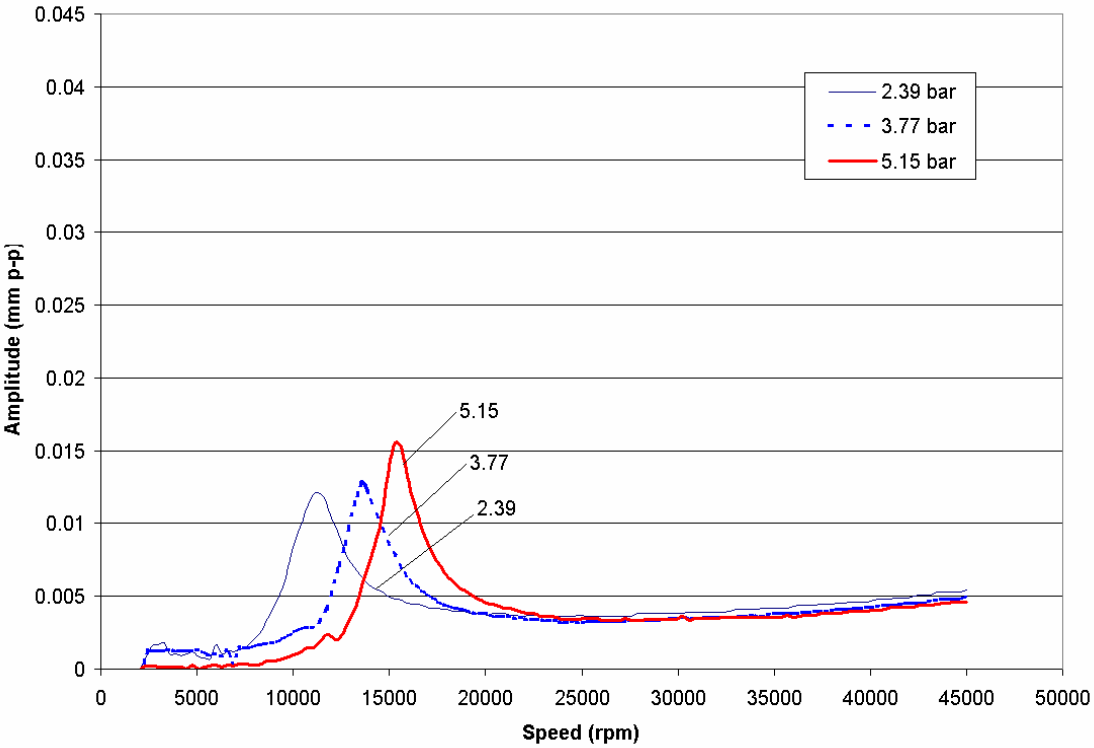

Figure 12 Baseline synchronous rotor p-p amplitudes versus rotor speed for three absolute feed pressures. Left bearing vertical displacements compensated for slow roll at 2076 rpm

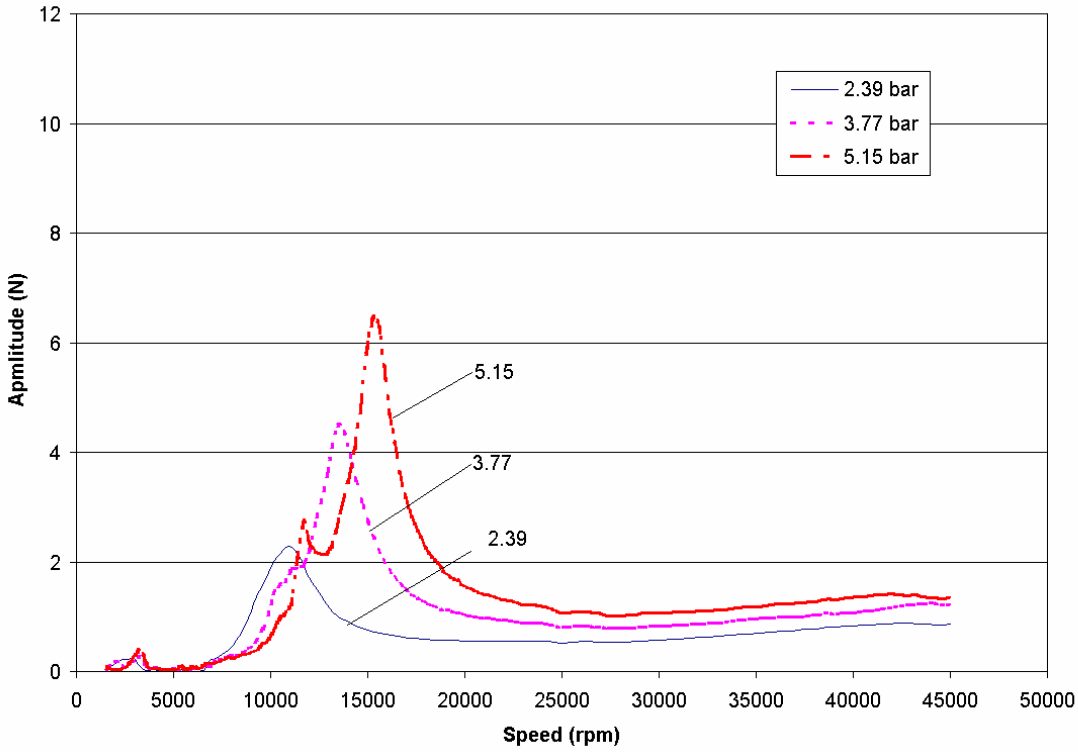

Figure 13 Baseline transmitted bearing force amplitudes versus rotor speed for three absolute supply pressures. Left bearing vertical load sensor

Calibrated Imbalance Responses

Calibrated cylindrical mode imbalance responses are obtained from the noted imbalance configurations, see Table 3 and Figure 6. Figures 14 and 15 depict the amplitudes of rotor motion and bearing transmitted load for a supply pressure equal to 3.77 bars (absolute). The displacements are slow-roll compensated at 2,000 rpm. The graphs show the responses at the left bearing (vertical plane) for the remnant imbalance and two calibrated imbalances, U_1 and U_2, respectively. Note that the added masses increase the critical speed from 13,700 rpm (baseline) to 14,400 rpm. Incidentally, the maximum amplitudes of motion are not necessarily proportional to the imbalance displacements since the remnant imbalance response has not been subtracted over the entire speed range. Rotor motion amplitudes and transmitted bearing forces at the other bearing (right) and at the horizontal plane are similar in magnitude, and not reproduced for brevity. Furthermore, the rotor responses did not show conditions of subsynchronous activity in any of the experiments.

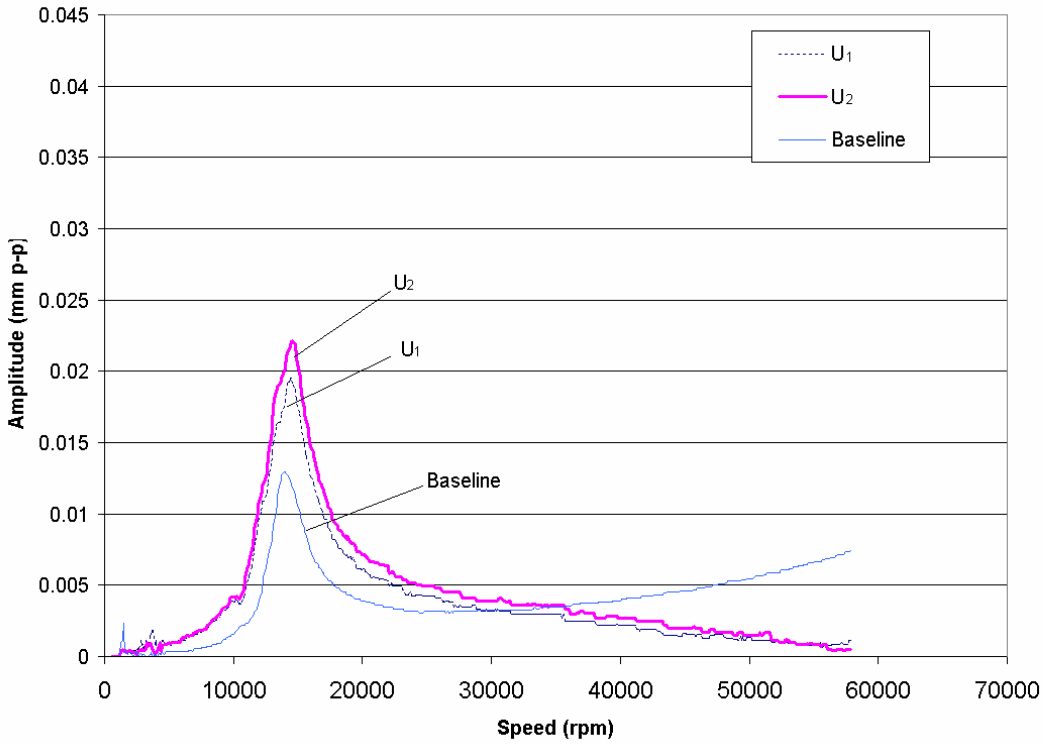

Figure 14 Synchronous peak to peak rotor amplitudes versus rotor speed for remnant imbalance and two imbalance conditions exciting cylindrical mode. Left bearing vertical displacements compensated for slow roll at 2000 rpm. Imbalances U_1=1.335 μm, U_2=1.567 μm. Supply pressure 3.77 bar (absolute)

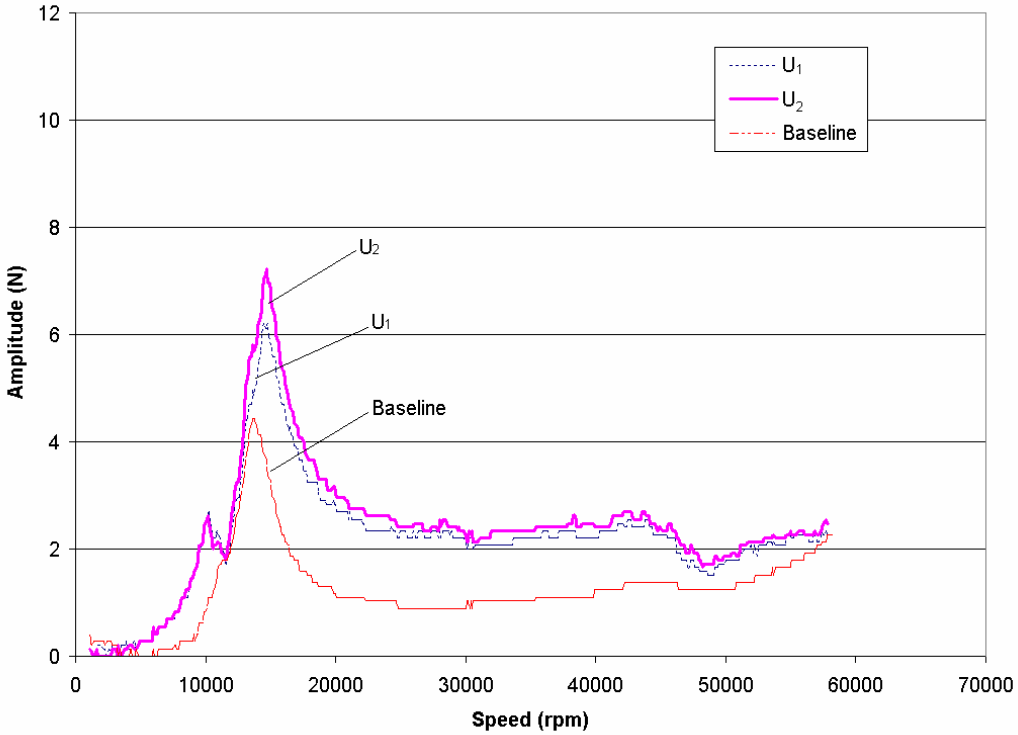

Figure 15 Amplitudes of transmitted bearing load versus rotor speed for remnant imbalance and two mass imbalances exciting cylindrical mode. Left bearing vertical force sensor. Imbalances U_1=1.335 μm, U_2=1.567 μm. Supply pressure 3.77 bar (absolute) [40 psig]

Figure 16 and 17 show the rotor amplitudes of motion and transmitted bearing load for the imbalance conditions exciting both the cylindrical and conical modes. The feed pressure equals to 3.77 bar (absolute). The conical mode imbalance distribution U_2', shown in Table 3 and Figure 7, determines larger amplitudes of motion in displacement and transmitted force than the cylindrical mode excitation U_1'.

For imbalance U_2', the rotor displacements while crossing the critical speed are at least 40 μm in magnitude, i.e. larger than the bearing nominal diametrical clearance of 40 μm. No rubbing conditions or instability are apparent from the measurements, see waterfall graph in Figure 18. The experimental measurements demonstrate the good tilting characteristic of the FPTPB. The transmitted force is the largest (~11 N) and more than twice the magnitude recorded from the baseline response.

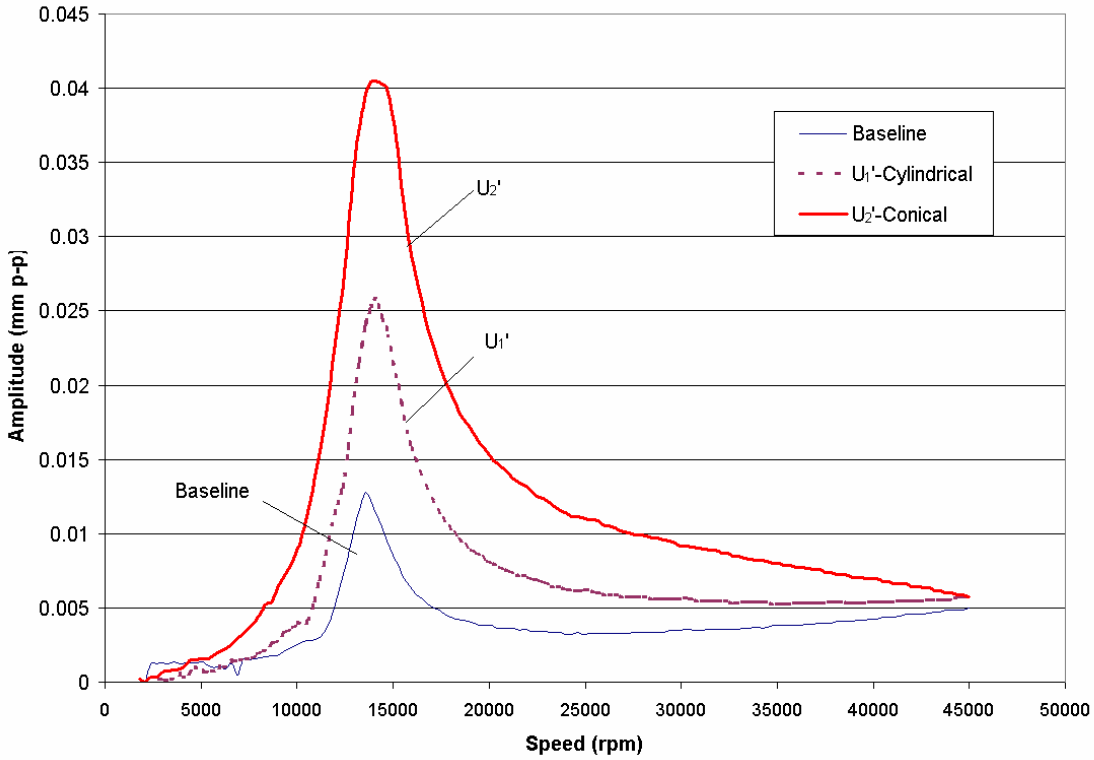

Figure 16 Synchronous peak to peak rotor amplitudes versus rotor speed for remnant imbalance and two imbalance conditions exciting combined cylindrical/conical modes. Left bearing vertical displacements compensated for slow roll at 2095 rpm. Imbalances U_1'=1.451 μm, U_2'=1.451 μm. Supply pressure 3.77 bar (absolute)

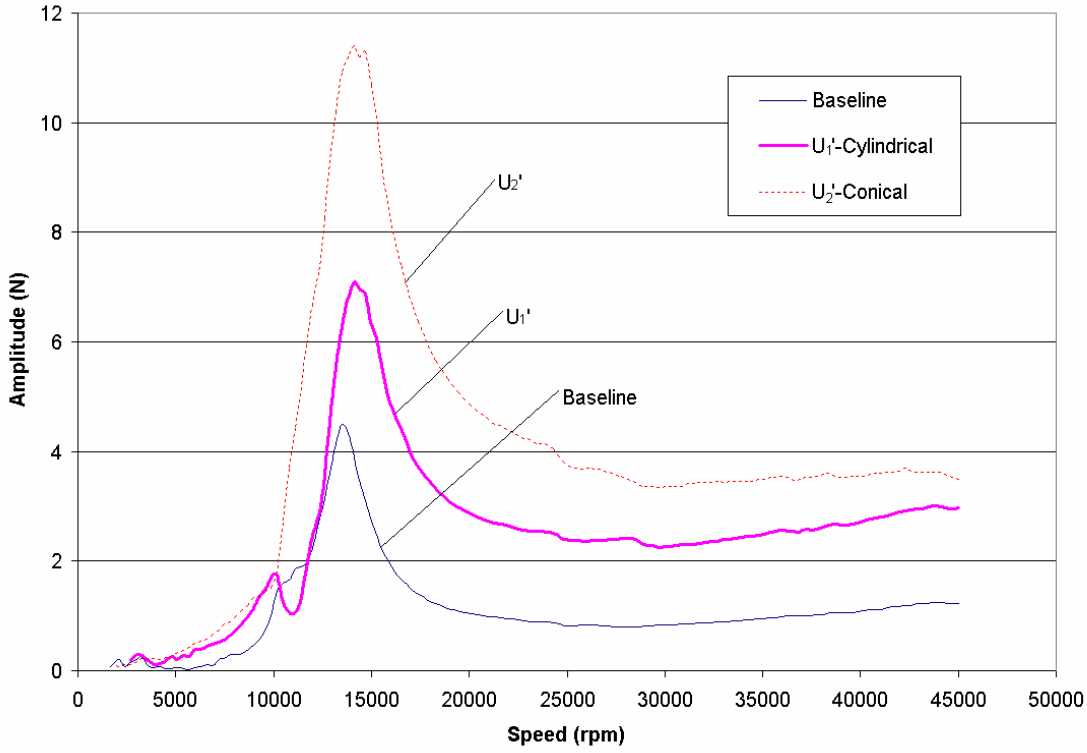

Figure 17 Transmitted amplitudes of bearing load versus rotor speed for remnant imbalance and two mass imbalances exciting combined cylindrical/conical modes. Left bearing vertical force sensor. Imbalances U_1'=1.451 μm, U_2'=1.451 μm. Supply pressure 3.77 bar (absolute)

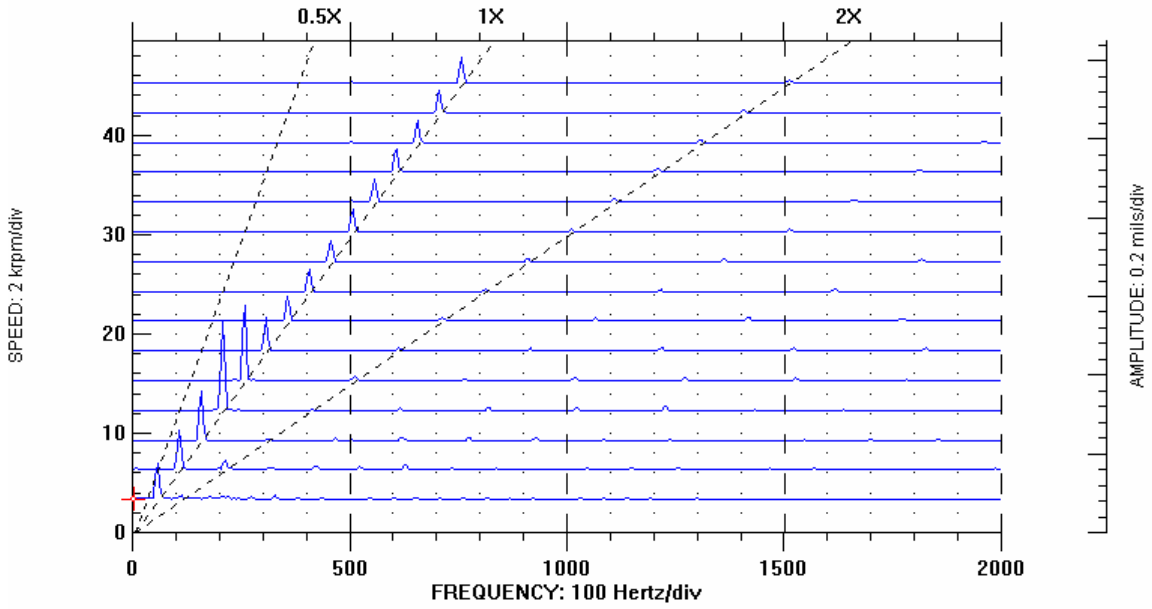

Figure 18 Waterfall plot of rotor amplitudes with conical imbalance excitation U_2'. At left bearing vertical plane (LV). Test at 3.77 bar absolute supply pressure

Estimation of damping ratios and equivalent stiffness for test gas bearings

The Q factor method is used to estimate the viscous damping ratio (ζ) of the rotor on its bearings. Figure 19 shows a typical rotor response and the nomenclature for application of the method. The Q-factor and damping ratio (ζ<0.1) are defined for slightly damped systems as:

$$Q = \frac{N_n}{N_2 - N_1} \qquad \zeta = \frac{1}{2Q} \tag{2}$$

The equivalent bearing stiffness (K_{eq}) is easily determined from the critical speed (ω_c) and the rotor mass shared by each bearing (M_1), i.e. $K_{eq} = M_1 \omega_c^2$. Table 4 presents the critical speeds, estimated damping ratio and equivalent stiffness for both bearings as determined from the rotor imbalance responses for the baseline condition and calibrated imbalance responses. Figure 20 shows the damping ratios decrease as the supply pressure increases. The estimated coefficients differ for each bearing and for each imbalance case since the rotor peak amplitude responses are large relative to the bearing radial clearance, thus denoting a degree of non linearity. It appears that an average of 10% damping ratio is adequate for most test conditions.

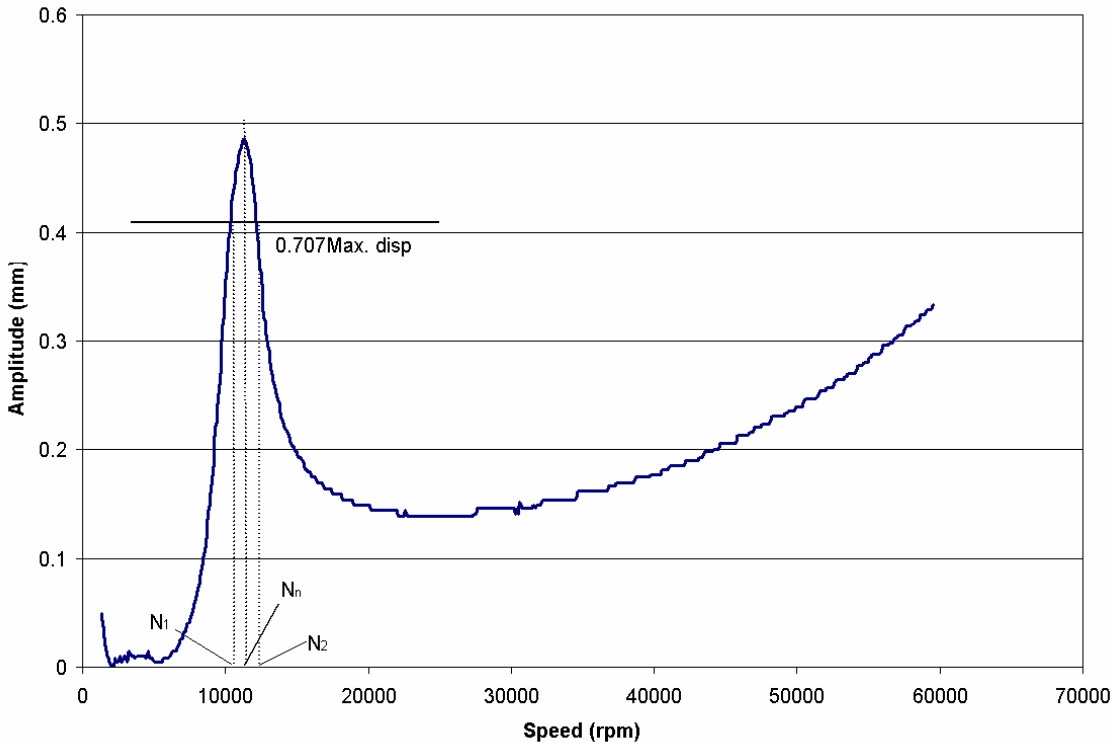

Figure 19 Typical rotor response and notation for application of Q-factor method and estimation of gas bearing damping ratio

Table 4 Estimated gas bearing damping ratio and equivalent stiffness from rotor imbalance responses

Displacement Sensor	Imbalance Conditions	Supply absolute Pressure (bar)	Critical Speed (rpm)	Damping Ratio (ζ)	K_{eq} (MN/m)
LV Bearing Left Vertical	Remnant	2.39	11,400	0.106	0.589
		3.77	13,500	0.089	0.826
		5.15	15,300	0.058	1.060
	U1’	2.39	11,700	0.090	0.621
		3.77	14,100	0.095	0.902
		5.15	15,890	0.076	1.140
	U2’	2.39	12,300	0.146	0.686
		3.77	14,100	0.117	0.902
		5.15	15,590	0.115	1.100
LH Bearing Left Horizontal	Remnant	2.39	10,800	0.111	0.529
		3.77	13,190	0.080	0.789
		5.15	15,000	0.080	1.020
	U1’	2.39	11,700	0.090	0.621
		3.77	14,100	0.053	0.902
		5.15	15,600	0.048	1.100
	U2’	2.39	11,990	0.113	0.652
		3.77	14,400	0.083	0.940
		5.15	16,500	0.082	1.230
RV Bearing Right Horizontal	Remnant	2.39	11,400	0.079	0.589
		3.77	11,100	0.081	0.559
		5.15	11,700	0.065	0.621
	U1’	2.39	9,300	0.161	0.392
		3.77	12,000	0.175	0.653
		5.15	11,700	0.077	0.621
	U2’	2.39	11,990	0.188	0.652
		3.77	14,100	0.138	0.902
		5.15	15,590	0.115	1.100
RH Bearing Right Horizontal	Remnant	2.39	11,400	0.119	0.589
		3.77	12,600	0.095	0.720
		5.15	14,100	0.117	0.902
	U1’	2.39	11,100	0.109	0.559
		3.77	13,790	0.087	0.862
		5.15	15,300	0.088	1.060
	U2’	2.39	11,990	0.100	0.652
		3.77	14,400	0.093	0.940
		5.15	14,700	0.132	0.980

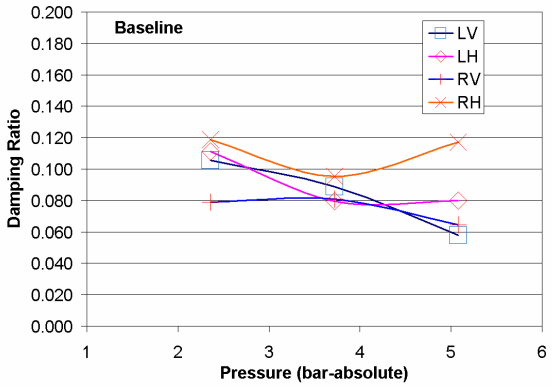

(a) Baseline response

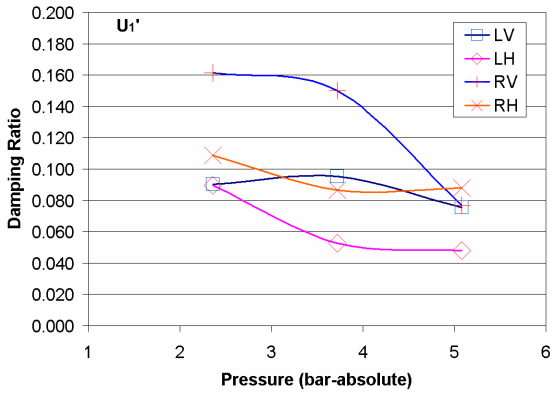

(b) Cylindrical mode imbalance response

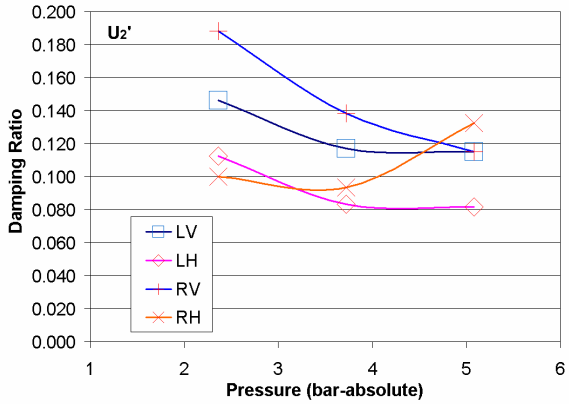

(c) Conical mode imbalance response

Figure 20 Estimated bearing damping ratios versus supply pressure (a) Baseline response, (b) Cylindrical mode imbalance response, (c) Conical mode imbalance (LV, LH): left bearing, horizontal and vertical planes, (RV, RH): right bearing, horizontal and vertical planes

Figure 21 shows that the equivalent gas bearing stiffnesses (K_{eq}) at the critical speed is linearly proportional to the (absolute) supply pressure, with the exception of the estimated coefficient for the right bearing, vertical plane motions. The stiffness ranges from about 0.6 MN/m to 1.2 MN/m (3,429 to 6,857 lb/in) as the supply pressure increases from two to five times the ambient magnitude. The drop in damping ratio is solely due to the increase in stiffness rather than a decrease in the physical damping magnitude. Figure 22 indicates the external supply pressure increases the gas bearing rotor system critical speed from 11.5 krpm to nearly 16 krpm.

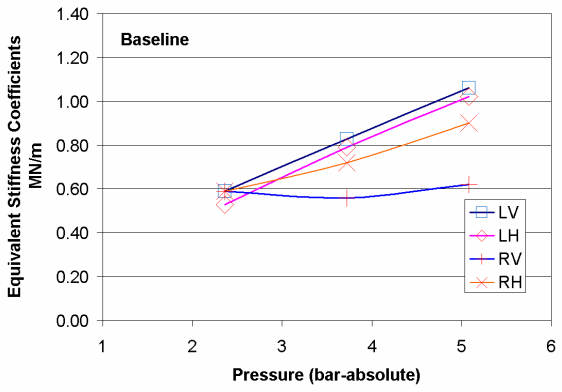

(a) Baseline response

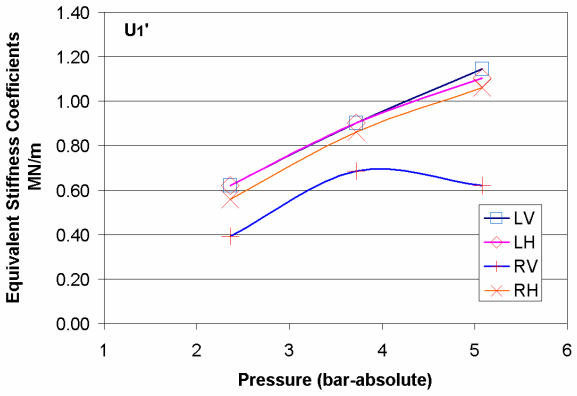

(b) Cylindrical mode imbalance response

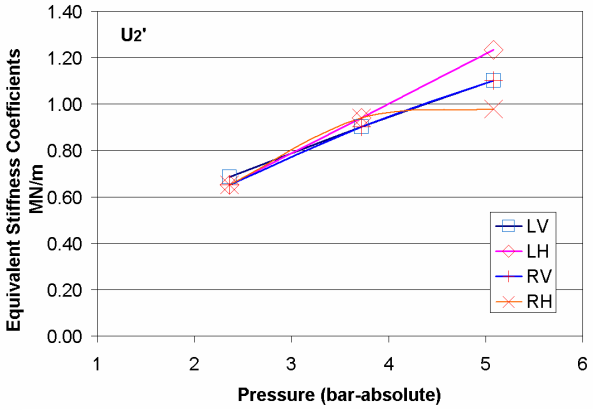

(c) Conical mode imbalance response

Figure 21 Estimated equivalent bearing stiffness versus supply pressure (a) Baseline response, (b) Cylindrical mode imbalance response, (c) Conical mode imbalance response (LV, LH): left bearing horizontal and vertical planes, (RV, RH): right bearing horizontal and vertical planes

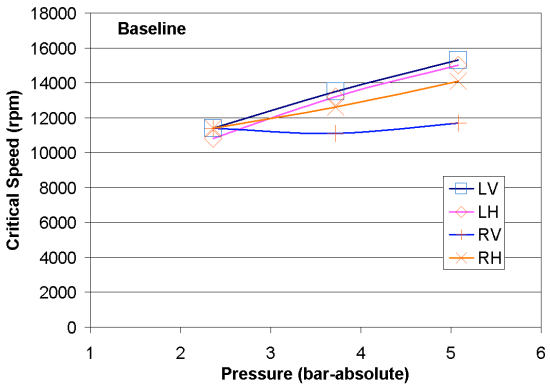

(a) Baseline response

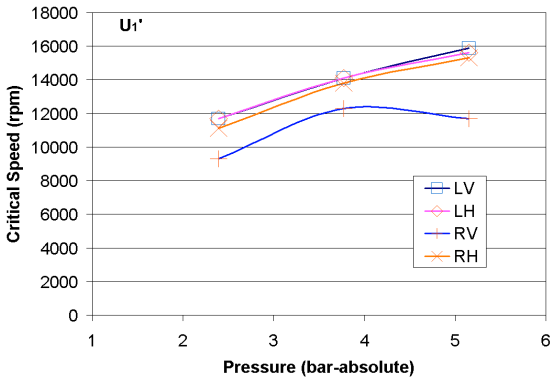

(b) Cylindrical mode imbalance response

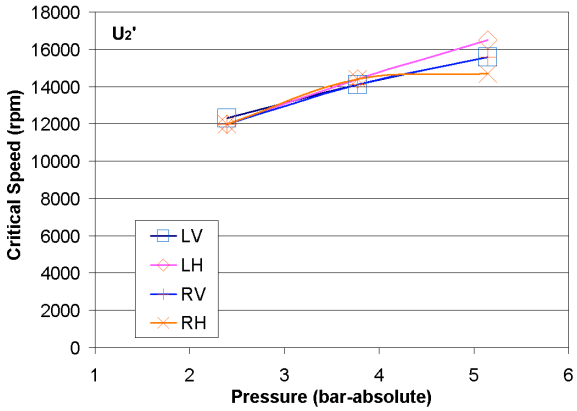

(c) Conical mode imbalance response

Figure 22 Rotor gas bearing system critical speed versus supply pressure (a) Baseline response, (b) Cylindrical mode imbalance response, (c) Conical mode imbalance response (LV, LH): left bearing horizontal and vertical planes, (RV, RH): right bearing horizontal and vertical planes

High speed tests to determine threshold speed of instability

The rotor mounted on the flexure pivot hydrostatic pad gas bearings shows dynamically stable responses to rotor speeds as high as 99,000 rpm[2], thus evidencing the test bearings provide little or negligible cross-coupled stiffness coefficients.

Experiments are conducted at rotor speeds well above the cylindrical rigid mode critical speed (~11 to 16 krpm). The external supply pressure is maintained at 3.77 bar (absolute [40 psig]) while the rotor passes through the critical speed and reaches the lowest test speed of 20 krpm. Next, the supply pressure lines are closed and the rotor runs up in speed to a top speed of 90,000 rpm. During this operating condition, the bearings are self-acting, i.e. work under a pure hydrodynamic fluid film regime.

The Labview® DAQ system collects the rotor displacements and loads. An ad-hoc MathCAD program processes the data and presents response amplitudes, whirl frequency ratio, and onset speed of instability, if applicable. In the experiments, the DAQ sampling rate is 10 kHz and a total of 2048 data points are collected from each sensor. The rotor speeds up from 20 krpm to 90 krpm and data is acquired each 1,000 rpm.

Figure 23 displays the synchronous rotor displacement and transmitted bearing loads versus increasing rotor speed for the condition of no external pressurization. Figure 24 depicts a waterfall of the rotor displacements, amplitudes and frequency content, as the speed ranges from low to high magnitudes. A rotor subsynchronous instability appears at a speed of 81,180 rpm (1353 Hz) and with a low whirl frequency equal to 271 Hz (16,260 rpm). The whirl frequency ratio is 0.20. Most importantly, however, the whirl frequency corresponds closely with the lowest critical speed (natural frequency) of the rotor on its bearings.

The rotor amplitudes of synchronous motion steadily increase with rotor speed and the forces show peak amplitudes at the threshold speed of instability (see Figure 23). Incidentally, the rotor orbits displayed in the oscilloscopes monitoring the overall response become larger and larger, and audible loud noise is characteristic as the rotor becomes unstable. Opening the air supply line and pressurizing the gas bearings immediately stabilized the rotor.

[2] Maximum speed allowable with current drive DC motor

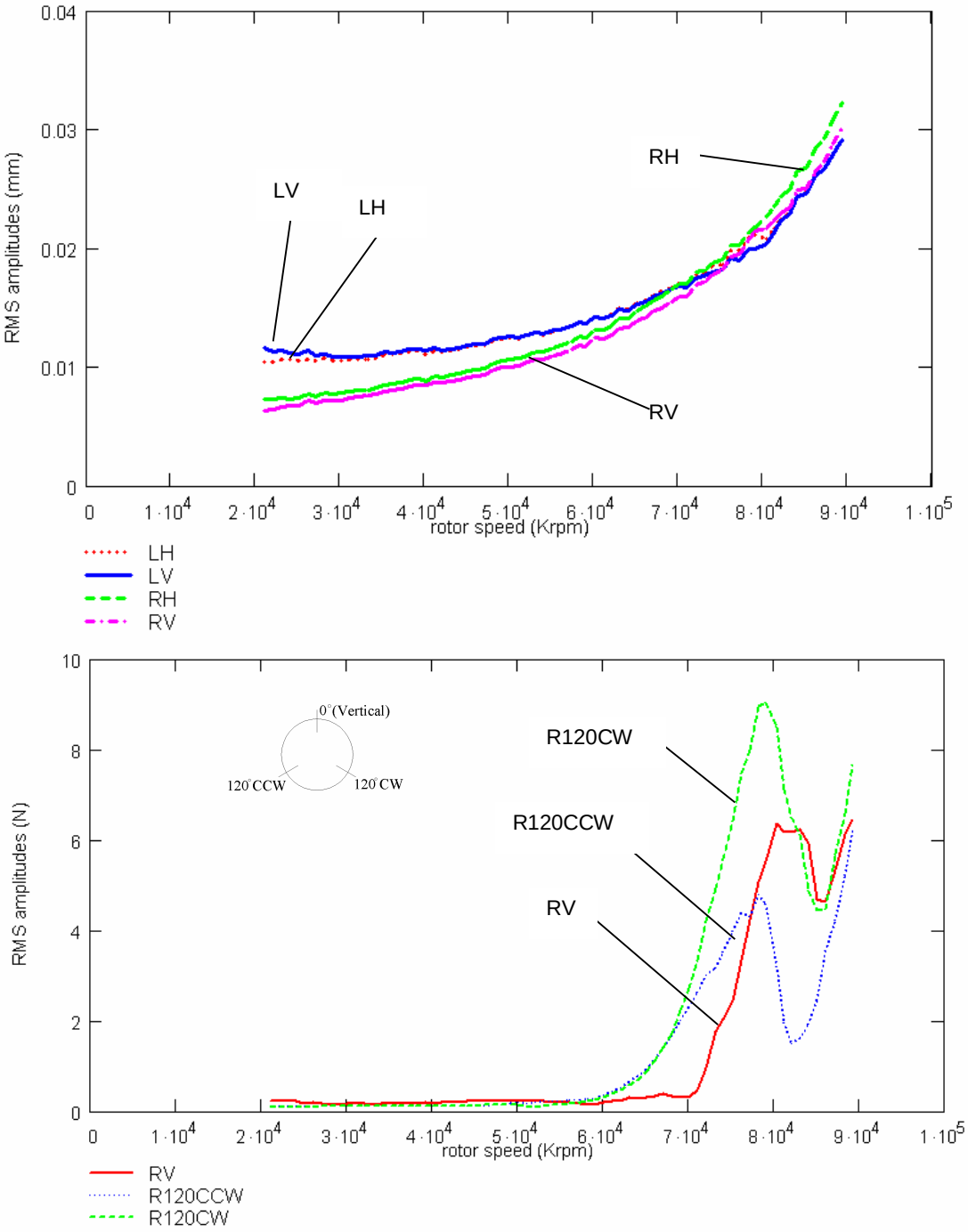

Figure 23 RMS synchronous amplitudes of rotor displacements and transmitted bearing loads in run-up tests to high speed. No feed pressure. (LV,LH): left bearing horizontal and vertical planes, (RV,RH): right bearing horizontal and vertical planes. Right bearing load sensors (three orientations)

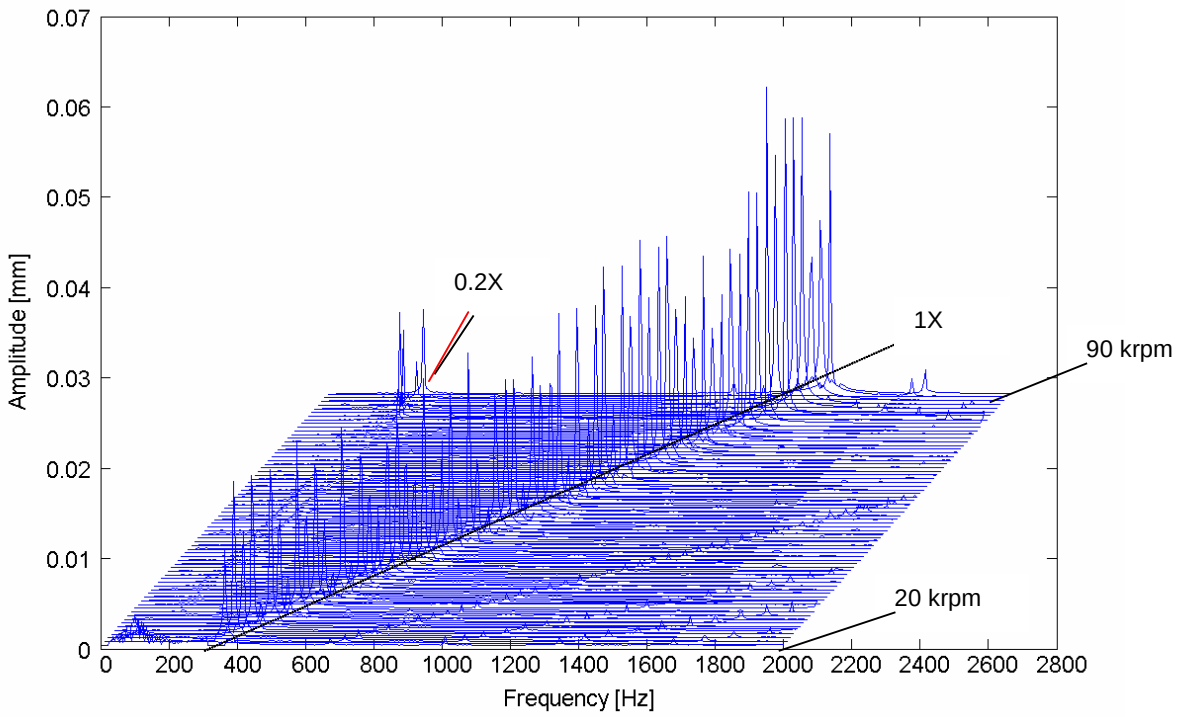

Figure 24 Waterfall plot of rotor amplitudes at right bearing vertical plane (RV). Run up test without external pressurization. Speed range 20 krpm to 90 krpm.

Each flexure pivot hydrostatic pad gas bearing contains eight feed orifices for external pressurization. In the tests described above, the four holes located between the pads were plugged and the other four orifices discharging into the pads were open. Thus, the operation of the bearing was truly of a hydrostatic/hydrodynamic character.

A series of experiments are conducted with the feed orifices into the pads plugged (no hydrostatic pad pressurization) and the orifices in between adjacent pads open. At first, the rotor would not lift with the four in-between pads supplied with external pressure. Apparently the discharge plenum has a large volume and the pressures acting on the rotor surface balance out and cannot lift the rotor. Next, the two top in-between pad orifices are plugged to provide a hydrostatic push upwards, thus ensuring rotor lift-off and avoidance of rotor rubbing at start up. The lift off supply pressure is 5.15 bars (absolute). However, when the rotor speed approached the lowest motor speed (10,400 rpm) severe subsynchronous amplitude motions become apparent. The subsynchronous instability gradually vanishes as the air supply pressure is reduced and eventually removed. This event shows that pneumatic hammer is the cause for the instability since the discharge curtain volume (between orifice end and rotor) is quite large.

Two tests followed under the conditions noted. One with rotor speeds increasing from 11 krpm to 50 krpm, and the other one for run up speeds from 40 krpm to 60 krpm. Figures 25 and 26 show the waterfall plots of amplitude of vibration and frequency content for both tests. The results correspond to the left bearing, vertical plane motions. In the first test, the rotor motion is mainly synchronous to the top speed of 50 krpm. However, in the second test,

a rotor subsynchronous instability appears at a speed of 58,040 rpm (967Hz) and with a low whirl frequency equal to 140 Hz (8,412 rpm). The whirl frequency ratio is ~ 0.15.

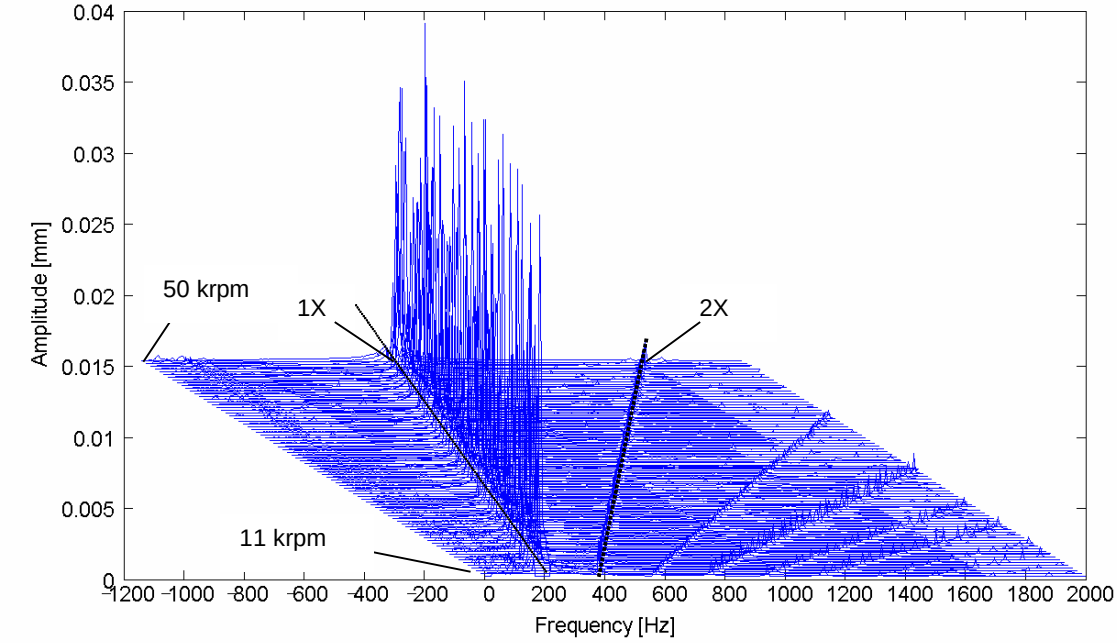

Figure 25 Waterfall plot of rotor amplitudes at left bearing, vertical plane (LV). Run up test without external pressurization. Pad orifices plugged. Speed range 11 krpm to 50 krpm

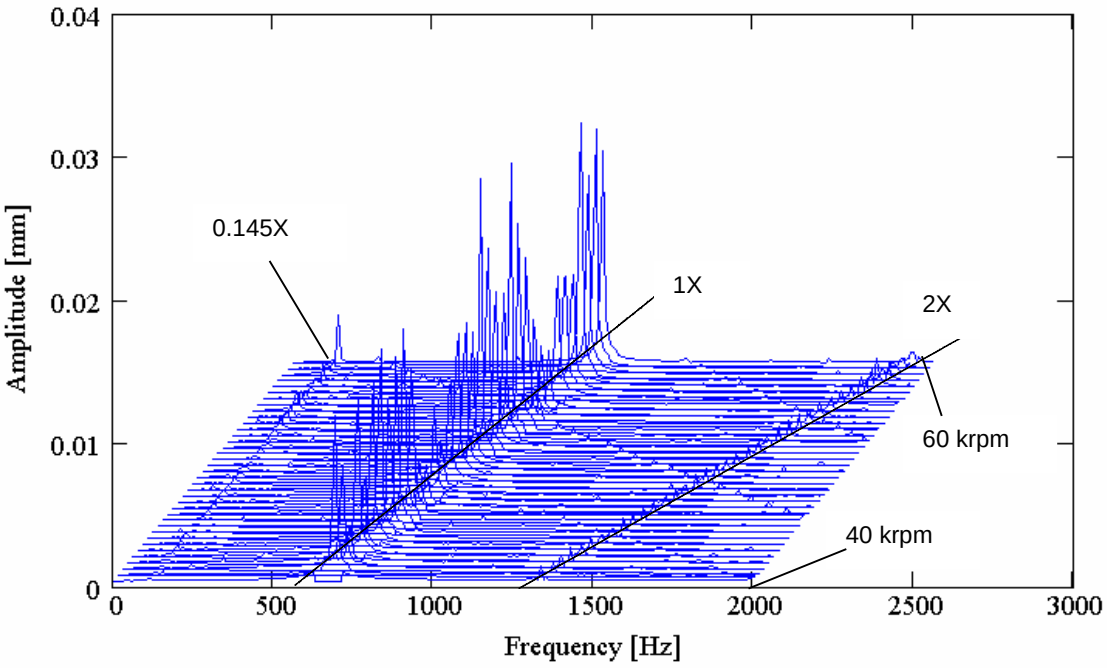

Figure 26 Waterfall plot of rotor amplitudes at left bearing, vertical plane (LV). Run up test without external pressurization. Pad orifices plugged. Speed range 40 krpm to 60 krpm

The threshold speed of instability (58 krpm) is much lower than the one obtained earlier (81.2 krpm). Both tests were conducted without external gas pressurization. However, by the time the last set of experiments finished, the rotor and bearings evidenced severe wear and sustained rub (increased clearances) due to the large motions apparent once the instability set in.

Lastly, a final without external pressurization and bringing the rotor quickly to a top speed above 60 krpm followed. Large amplitude subsynchronous motions were apparent while the rotor banged against the bearing walls. The severe vibrations could not be suppressed. The thermocouple monitoring the motor armature showed a rapid raise in temperature (115 F). The test terminated when the motor drive fuse burnt. The high temperature resulted in burning the coating on the shaft surface and visible smoke was evident. Post test inspection of the rotor and bearings shows extreme wear and debris resultant from the severe rubbing and sustained impacting when the rotor went unstable.

Identification of bearing dynamic force coefficients

In the experiments, rotor displacements and bearing transmitted forces are recorded. Thus, synchronous bearing force coefficients can be easily estimated from the imbalance response data. Since the test gas bearings offer little cross-coupling stiffnesses, the method simplifies to an estimation of the transfer function, load over displacement, and from which the bearing stiffness and damping can be obtained. Let (F_X, F_Y) be the synchronous components of the transmitted forces, and (X, Y) be the complex amplitudes of motion. Then, the force coefficients, direct damping and stiffness, can be obtained from the fundamental relationships:

$$K_{XX} + i\omega C_{XX} = \frac{F_X}{X}; \quad K_{YY} + i\omega C_{YY} = \frac{F_Y}{Y} \tag{3}$$

where (ω) is the frequency synchronous with rotor speed. Note that in the identification procedure, vector load addition is used to determine the vertical (Y) and horizontal (X) transmitted loads from the measured loads at the three circumferential locations, 120 degree apart.

Imbalance response measurements are performed with coast-down tests from 45 krpm and three supply pressures equal to 2.39, 3.77 and 5.15 bar (absolute). Two different imbalance excitations, cylindrical and conical modes, are considered at each supply pressure.

Figure 27 shows the identified synchronous speed direct stiffness (K_{XX}) and damping (C_{XX}) coefficients for the three test supply pressures. Figure 28 depicts the direct stiffness (K_{YY}) and damping (C_{YY}) coefficients. The results correspond to the left bearing in the test rig, and X and Y denote the vertical and horizontal directions. In general, the direct stiffnesses increase both with pressure supply and rotor speed. The estimated coefficients correlate well with the equivalent stiffnesses determined from the critical speeds, see Figure 21. On the other hand, the direct damping coefficients show an erratic behavior with rotor speed, though decreasing in magnitude as the feed pressure increases. Note that the physical magnitude of the damping coefficients is small.

It is of importance to note that a multiplicative constant equal to 2.5 was used to bring the identified stiffness and damping coefficients in agreement with those determined from the Q-factor method. The rationale lies in that the recorded transmitted forces are a fraction of the actual ones since each bearing was installed with a stiff alignment mechanism that acted as an additional radial load path. This oversight in the assembly process will be corrected in future experiments.

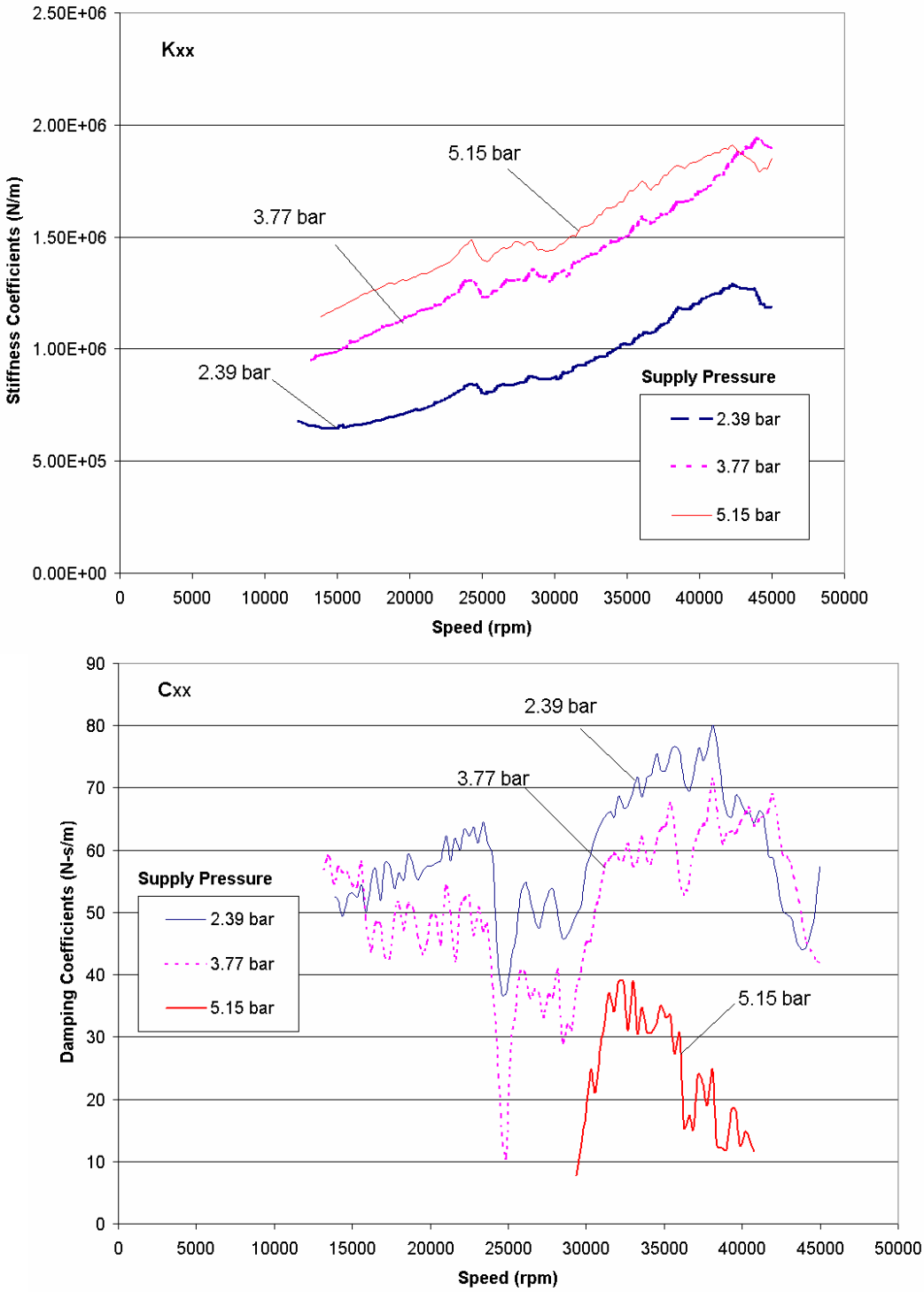

Figure 27 Estimated gas bearing direct stiffness and damping coefficients (K_{XX}, C_{XX}) versus rotor speeds for three supply pressures. Synchronous speed force coefficients. X-vertical

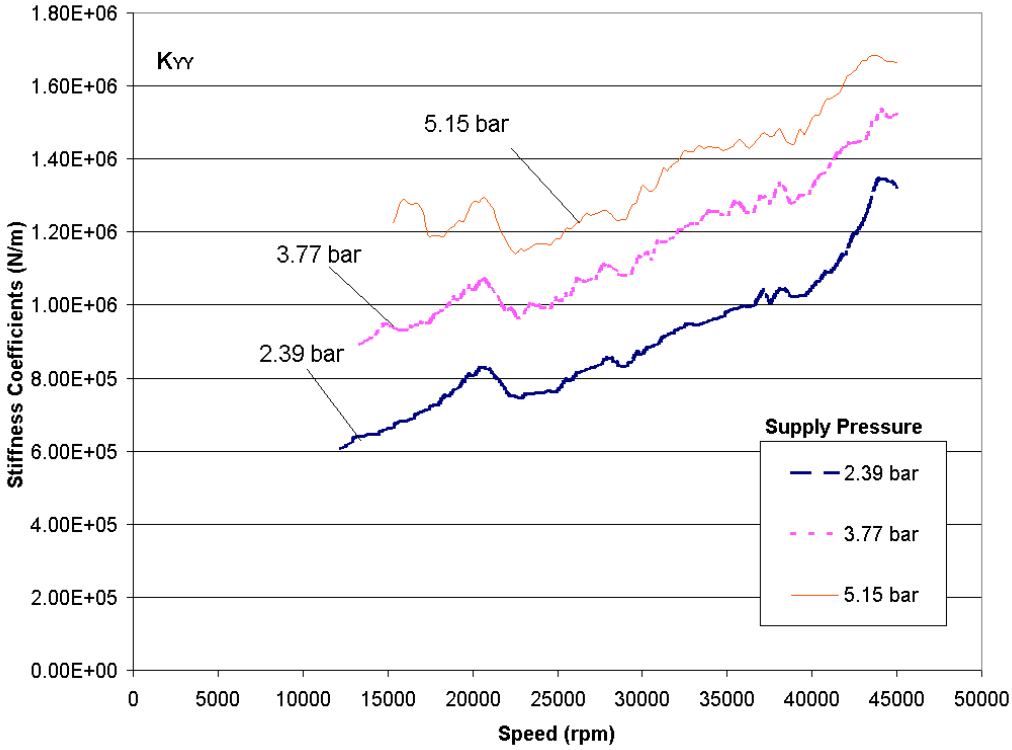

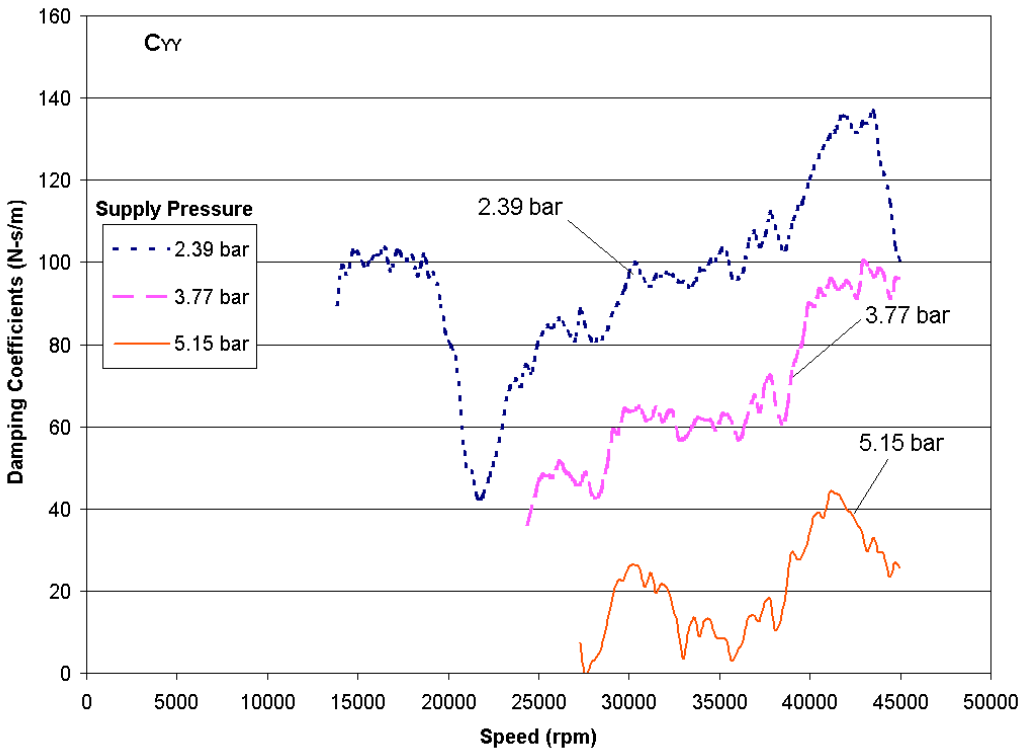

Figure 28 Estimated gas bearing direct stiffness and damping coefficients (K_{YY}, C_{YY}) versus rotor speeds for three supply pressures. Synchronous speed force coefficients. Y-horizontal

Prediction of gas bearing dynamic force coefficients

TPGASBEAR is a FORTRAN computer program determining the static and dynamic forced response of flexibly mounted – multiple pad gas bearings and seals [24]. A visual interface in EXCEL handles the user input and FORTRAN program output calculations.

The computational finite difference analysis solves the Reynolds equation for gas films, i.e.

$$\frac{1}{R^2}\frac{\partial}{\partial\theta}\left(\frac{P\cdot h^3}{12\cdot\mu}\frac{\partial P}{\partial\theta}\right)+\frac{\partial}{\partial z}\left(\frac{P\cdot h^3}{12\cdot\mu}\frac{\partial P}{\partial z}\right)=\frac{\Omega}{2}\frac{\partial}{\partial\theta}(P\cdot h)+\frac{\partial}{\partial t}(P\cdot h) \qquad (4)$$

Small amplitude rotor motions about an equilibrium position lead to a nonlinear partial differential equation for the static pressure field, and a set of first order linear partial differential equations for perturbed pressures. The first order pressure fields determine the rotordynamic force coefficients, stiffness and damping, as function of the excitation frequency and other operating conditions. San Andrés [25] describes in detail the analysis and numerical method, as well as predictions of force coefficients for brush seals with reverse rotation ability.

Table 5 presents the dimensions and operating conditions for the FPTPBs and used as input into the predictive computer program. Note the change in bearing preload and clearance, which were determined from measurements in the laboratory. Also recall that TPGASBEAR can not currently account for the hydrostatic feed pressurization into the pads.

Table 5 Geometry of flexure-pivot gas bearing (4 pads, LOP)
Static load = 4.05 N

Parameter	*Magnitude*
Rotor diameter, D	28.48 mm
Bearing axial length, L	33.2 mm
Measured radial clearance, C	0.030 mm
Dimensionless pad preload, r	0.27
Pad pivot (offset)	60%
Pad arc length	72 degrees
Gas constant, $\mathfrak{R}$	286.7 J/Kg-K (air)
Temperature	26.7 °C
Viscosity, μ	1.85x 10^{-6} Pa-s
Density, ρ_A	1.16 kg/m^3
Ambient pressure, P_A	1 bar

Pad mass and inertia coefficients ~ negligible

PAD Stiffness Matrix

Moment	20	0	0	pad rotation angle
normal F	0	10^8	0	Normal displacement
transverse F	0	0	10^8	Transverse displacement

Number of grid points (pad): 17 circumferential, 11 axial
Convergence criteria (pressure difference) = 10^{-5} Pa

The flexural web in the FPTPB provides nearly rigid radial and transverse stiffnesses, i.e. $K^S_{\xi\xi} = K^S_{\eta\eta} \to \infty$, and the moment stiffness $K^S_{\delta\delta}$ = 20 Nm/rad is known from the bearing provider. The static load on each bearing equals 4.05 N and the rotor speed varies from 10 krpm to 80 krpm.

Figure 29 displays the spreadsheet with the major parameters for description of the bearing. Each cell displays a descriptive comment of its content (input and output). The interface offers two major options:

a) given rotor eccentricity, find reaction forces and force coefficients,
b) given the applied load, find rotor eccentricity and force coefficients.

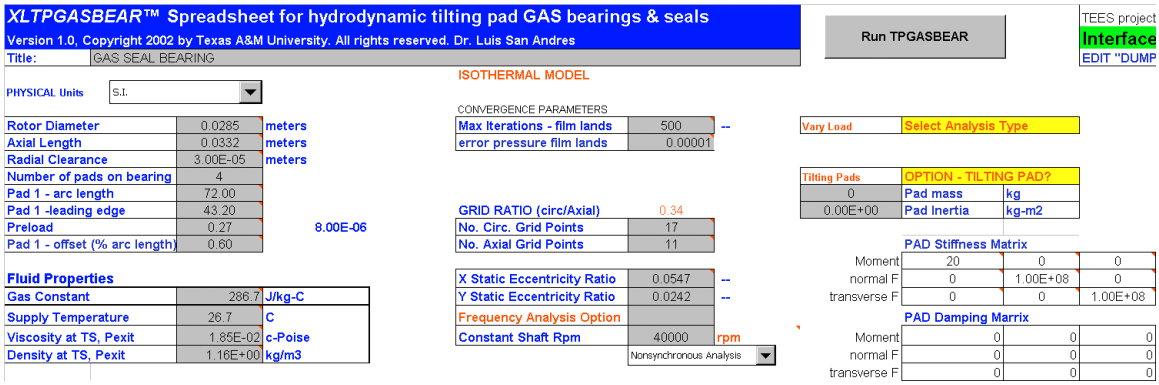

XLTPGASBEAR™ Spreadsheet for hydrodynamic tilting pad GAS bearings & seals

Version 1.0, Copyright 2002 by Texas A&M University. All rights reserved. Dr. Luis San Andres

Run TPGASBEAR

TEES project: Interface

EDIT "DUMP

Title: GAS SEAL BEARING

ISOTHERMAL MODEL

PHYSICAL Units: S.I.

CONVERGENCE PARAMETERS

Rotor Diameter	0.0285	meters
Axial Length	0.0332	meters
Radial Clearance	3.00E-05	meters
Number of pads on bearing	4	
Pad 1 - arc length	72.00	
Pad 1 -leading edge	43.20	
Preload	0.27	8.00E-06
Pad 1 - offset (% arc length)	0.60	

Max Iterations - film lands	500	--
error pressure film lands	0.00001	

Vary Load	Select Analysis Type

Tilting Pads	OPTION - TILTING PAD?	
0	Pad mass	kg
0.00E+00	Pad Inertia	kg-m2

Fluid Properties

Gas Constant	286.7	J/kg-C
Supply Temperature	26.7	C
Viscosity at TS, Pexit	1.85E-02	c-Poise
Density at TS, Pexit	1.16E+00	kg/m3

GRID RATIO (circ/Axial)	0.34	
No. Circ. Grid Points	17	
No. Axial Grid Points	11	

X Static Eccentricity Ratio	0.0547	--
Y Static Eccentricity Ratio	0.0242	--
Frequency Analysis Option		
Constant Shaft Rpm	40000	rpm
	Nonsynchronous Analysis	

PAD Stiffness Matrix

Moment	20	0	0
normal F	0	1.00E+08	0
transverse F	0	0	1.00E+08

PAD Damping Marrix

Moment	0	0	0
normal F	0	0	0
transverse F	0	0	0

Figure 29 Input data in worksheet for hydrodynamic analysis of tilting pad gas bearing

Force coefficients are calculated for a range of operating speeds and synchronous whirl frequencies or for a number of whirl frequencies keeping the rotor speed constant. Figure 30 displays in tabular form, as a function of rotor speed, the calculated force coefficients and other static performance characteristics, i.e. flow rate, power loss, maximum pressure, etc. The interface creates graphs depicting the variation of the predicted parameters (stiffness and damping coefficients, flow rate, drag torque and power loss) versus the rotor speed or whirl frequency (whichever is appropriate).

P Supply bars	P Exit bars	Load-X N	Load-Y N	Speed rpm	Kxx N/m	Kxy N/m	Kyx N/m	Kyy N/m	Cxx N-s/m	Cxy N-s/m	Cyx N-s/m	Cyy N-s/m
1.00E+00	1.00E+00	4.056	0	80000	1926600	239270	-258180	1935700	152.03	-91.024	90.504	154.91
1.00E+00	1.00E+00	4.056	0	60000	1584200	320850	-326020	1591300	188.84	-106.6	103.32	188.48
1.00E+00	1.00E+00	4.056	0	40000	1.12E+06	4.00E+05	-3.54E+05	1.16E+06	260.3	-122.32	113.84	248.26
1.00E+00	1.00E+00	4.056	0	20000	5.62E+05	4.24E+05	-2.18E+05	8.67E+05	391	-113	153	368
1.00E+00	1.00E+00	4.056	0	10000	5.20E+05	4.00E+05	-5.55E+04	1.06E+06	536.01	-98.374	357.04	523.36

Speed rpm	ex/C [-]	ey/C [-]	Mass Flow kg/s	Fx Reaction N	Fy Reaction N	Power Loss kW	Keq N/m	WFR	Torque N.m	Force N	Angle	Max pressure bar
80000	0.0589	0.0648	-3.473E-06	-4.076E+00	-3.421E-03	2.78E-02	1.78E+06	0.1934	3.32E-03	4.08E+00	0.0000	1.1518
60000	0.0657	0.0803	-2.469E-06	-4.059E+00	1.974E-03	1.57E-02	1.41E+06	0.2728	2.50E-03	4.06E+00	0.0000	1.1321
40000	0.0821	0.1191	-1.394E-06	-4.058E+00	-9.954E-04	7.09E-03	9.67E+05	0.3525	1.69E-03	4.06E+00	0.0000	1.1104
20000	0.1452	0.2402	-5.232E-07	-4.057E+00	6.308E-03	1.90E-03	6.01E+05	0.3408	9.08E-04	4.06E+00	0.0000	1.0995
10000	0.2642	0.3831	-2.563E-07	-4.057E+00	-7.519E-04	5.64E-04	6.52E+05	0.0000	5.39E-04	4.06E+00	0.0000	1.1138

Figure 30 Example of output predictions from hydrodynamic analysis of tilting pad gas bearing

Figure 31 depicts the (dimensionless) hydrodynamic pressure field at a rotor speed of 40 krpm for a predicted journal eccentricity, e_X/C=0.089 and e_Y/C=0.119, required to balance the static load. Figures 32 show the journal eccentricity components and drag power versus rotor

speed for the applied (static) load of 4.05 N. The journal eccentricity component *(Y)*, transverse to the load direction *(X)*, is slightly larger than the *(X)* component, thus denoting a degree of cross coupling in the FPTPB. Note the rotor approaches the centered condition, null eccentricity, as the speed increases. The bearing drag power is quite small, a few watts, and proportional to the rotor speed to the power two.

Figure 33 displays the bearing synchronous stiffness and damping force coefficients versus rotor speed. These force coefficients are evaluated at a frequency coinciding with the rotor angular speed in cycles/sec, and thus are appropriate to conduct imbalance response predictions of the rotor-gas bearing system. The cross-coupled stiffness coefficients are in general small while the direct stiffness coefficients increase with rotor speed. The direct damping coefficients, on the other hand, decrease rapidly as the rotor speed increases denoting a reduction in the ability of the gas bearing to attenuate high frequency vibrations

Figure 34 depicts the effect of excitation frequency on the force coefficients for operation at a rotor speed of 40 krpm. In the graphs, the vertical lines mark the excitation frequency coinciding with rotor speed. Note that the direct stiffness coefficients increase rapidly with frequency showing the typical gas bearing hardening effect. On the other hand, the direct damping coefficients reduce dramatically as the excitation frequency raises. Cross-coupled stiffness coefficients show a similar behavior. It is well known that at high excitation frequencies, gas bearings become quite stiff with little or no viscous-damping coefficients. This phenomenon is currently taken to advantage in the design and operation of honeycomb gas seal, for example [26].

The predictions show the FPTPB has a whirl frequency ratio of about 0.30 for high speed operation (> 30 krpm). However, since the gas bearing direct stiffnesses increase with speed, the rotor-bearings system natural frequency also raises thus delaying the onset of a hydrodynamic instability.

Figure 35 shows a comparison between the predicted synchronous direct force coefficients and the experimentally derived direct stiffness and damping coefficients. The test coefficients are determined from the imbalance response measurements and the lowest feed pressure of 2.39 bar (absolute), see Figures 27 and 28. Cross-coupled effects are regarded as minimal for the test bearing configuration with external pressurization.

The predicted stiffnesses match well the experimentally identified coefficients, in particular at high rotor speeds where hydrodynamic effects dominate the fluid flow in the bearing. Test direct damping coefficients are substantially smaller than the predicted coefficients. These results are demonstrative of the limited damping characteristics of gas bearings.

.

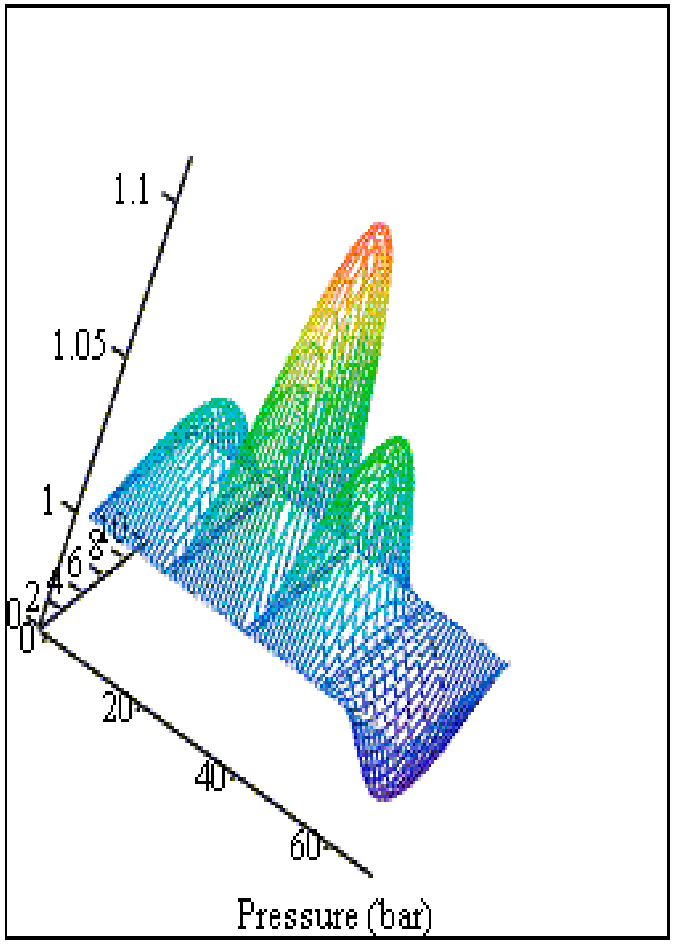

P

Figure 31 Predicted hydrodynamic pressure field for flexure pivot gas bearing at 40 krpm. Static load = 4.05 N, e_X/C=0.082, e_Y/C=0.119

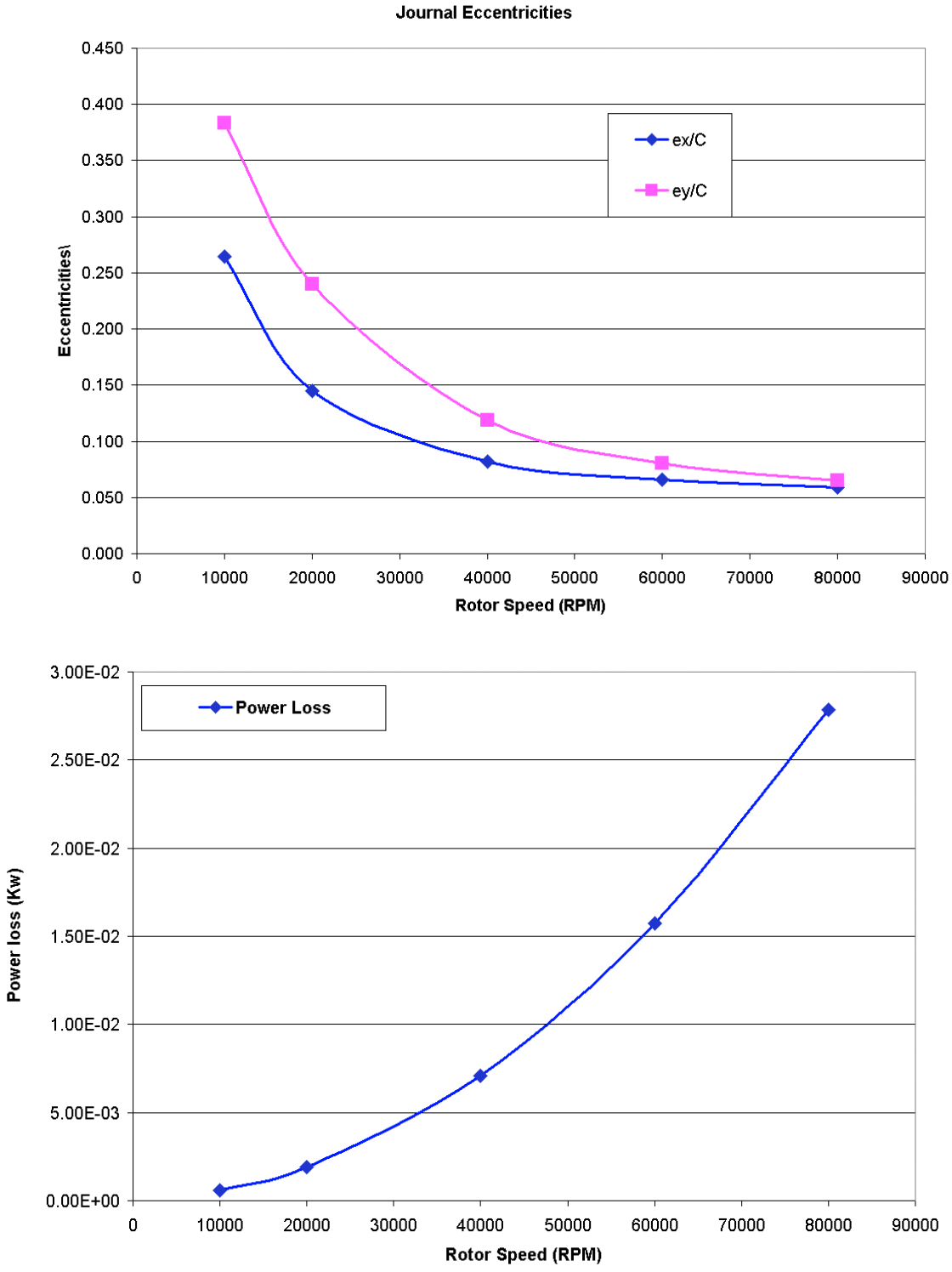

Figure 32 Predicted journal eccentricities (e/C) and power loss versus rotor speed for tilting pad gas bearing

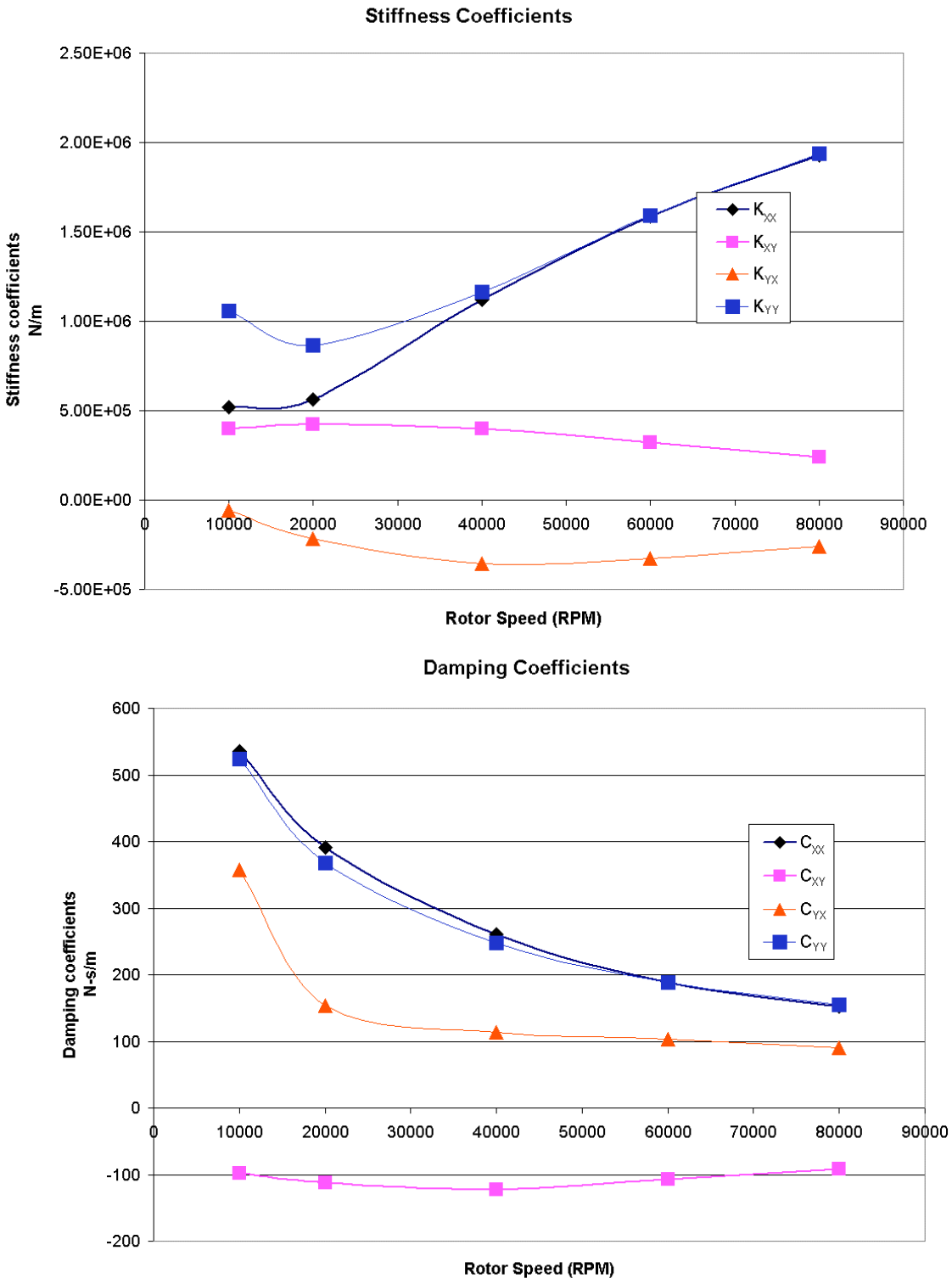

Figure 33 Predicted synchronous stiffness and damping force coefficients versus rotor speed for tilting pad gas bearing

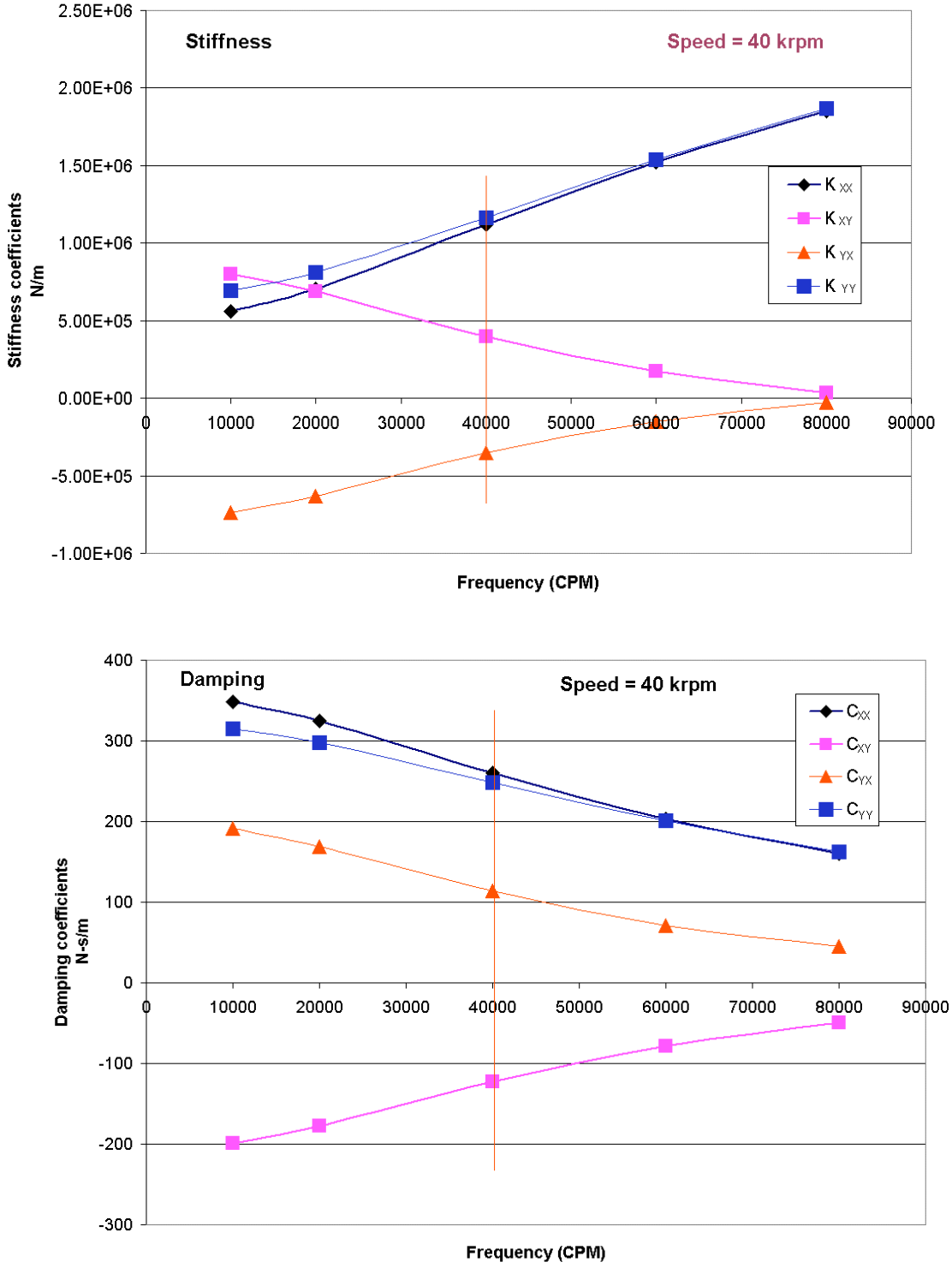

Figure 34 Effect of excitation frequency on predicted gas bearing force coefficients. Rotor speed = 40 krpm

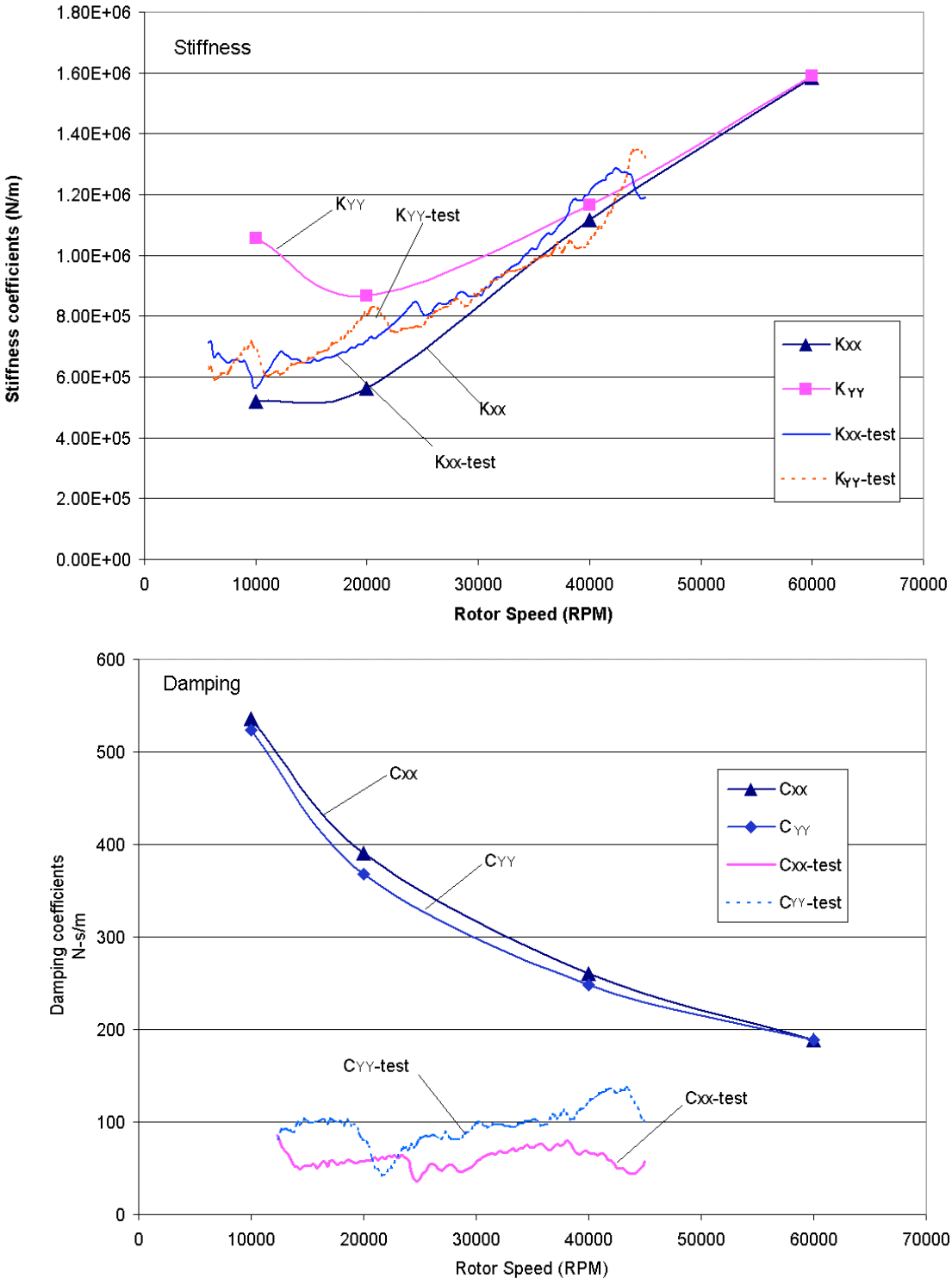

Figure 35 Comparison of predicted and experimentally identified synchronous direct stiffness and damping force coefficients for gas bearing

Conclusions

Comprehensive experiments conducted on a test rotor supported on hybrid flexure pivot – tilting pad bearings (FPTPBs) demonstrate their excellent stability characteristics and ability to carry dynamic loads. Imbalance experiments were conducted for feed pressures up to five times ambient and for rotor speeds as high as 99,000 rpm. The rotordynamic performance of the FPTPBs is superior to that of pressurized three-lobe cylindrical bearings tested earlier [2], and which showed severe subsynchronous instabilities, irrespective of the feed pressure.

The extensive imbalance response measurements demonstrate that the hydrostatic pressure increases the gas bearings' direct stiffness coefficients and raises the fundamental rotor-bearings system critical speed. The viscous damping ratios determined from the rotor peak response at its critical speed decreases as the feed pressure increases. Predictions for direct stiffness correlate well with experimentally identified synchronous force coefficients. Test damping coefficients are about 50% or less of the predicted magnitudes.

Measurements without external feed pressure show the onset of a subsynchronous instability at about 81 krpm with a whirl frequency ratio of 20%. The instability caused large (harmful) amplitude motions with the rotor rubbing on its bearings. Further tests with the bearings operating in a pure hydrodynamic mode evidenced a violent subsynchronous instability at a lower rotor speed, ~ 58 krpm. Sustained operation under these conditions caused severe wear and permanent loss of the protective (Teflon) coating.

Predictions for hydrodynamic operation show the paramount effect of excitation frequency on the bearing dynamic force coefficients, stiffness and damping. Further work is proposed to enhance the analysis by incorporating the feed pressure and orifice gas flow equations into the tilting pad bearing computational program.

The experiments and analysis advance the application of gas bearings for oil-free turbomachinery applications. FPTPBs are mechanically complex and costlier than cylindrical plain bearings. However, their enhanced stability characteristics and predictable rotordynamic performance makes them desirable for the envisioned oil-free applications in high speed micro turbomachinery.

References

[1] Lund, J. W., 1967, “A Theoretical Analysis of Whirl Instability and Pneumatic Hammer for a Rigid Rotor in Pressurized Gas Journal Bearings”, ASME Journal of Lubrication Technology, Vol. 89, pp. 154-163.

[2] Wilde, D.A., and San Andrés, L., 2003, “Experimental Response of Simple Gas Hybrid Bearings for Oil-Free Turbomachinery,” ASME Paper GT 2003-38833.

[3] Zeidan, F.Y., 1992, “Developments in Fluid Film Bearing Technology,” Turbomachinery International, pp. 24-31.

[4] Denhard, W. G., and Pan, C. H. T., 1968, “Application of Gas-Lubricated Bearings to Instruments”, ASME Journal of Lubrication Technology, Vol. 90, pp. 731-739.

[5] Wong, R. Y., Stewart, W. L., and Rohlok, H. E., 1968, “Pivot-Pad Journal Gas Bearing Performance in Exploratory Operation of Brayton Cycle Turbocompressor”, ASME Journal of Lubrication Technology, Vol. 90, pp. 687-700.

[6] Fuller, D. D., 1969, “ A Review of the State-of-the-Art for Design of Self-Acting Gas-Lubricated Bearing”, ASME Journal of Lubrication Technology, Vol. 91, pp. 1-16.

[7] Elwell, R. C., and Findlay, J. A., 1969, “Design of Pivoted Pad Journal Bearings”, ASME Journal of Lubrication Technology, Vol. 91, pp. 87-103.

[8] Lund, J. W. 1968, “Calculation of Stiffness and Damping Properties of Gas Bearings”, ASME Journal of Lubrication Technology, Vol. 90, pp. 793-803.

[9] Lund, J. W., and Pederson, L. B., 1987, “The Influence of Pad Flexibility on the Dynamic Coefficients of a Tilting Pad Journal Bearing”, ASME Journal of Lubrication Technology, Vol. 109, pp. 65-70.

[10] Chen, W. J., Zeidan, F. Y., and Jain, D., 1994, “Design, Analysis and Testing of High Performance Bearing in a High Speed Integrally Geared Compressor”, Proceeding of the 23rd Turbomachinery Symposium, pp. 31-42.

[11] Armentrout, R. W., and Paquette, D. J., 1993, “Rotordynamic Characteristics of Flexure-Pivot Tilting-Pad Journal Bearings”, STLE Tribology Transactions, Vol. 36, pp. 443-451.

[12] Kepple, W. E., Read, D. W., and Zeidan, F. Y., 1998, “Experience in the Use of Flexure Pivot Tilt Pad Bearings in Boiler Feedwater Pumps”, Proceeding of the 15th International Pump Users Symposium, pp. 77-83.

[13] Agahi, R., Ershaghi, B., and Zeidan, F. Y., “Application of High Speed and High Efficiency Hydrogen Turboexpanders in Refinery Service”, Proceedings of the 25th Turbomachinery Symposium, pp. 95-101.

[14] Castelli, V., and Elrod, H. G., 1965, “Solution of the Stability Problem for 360 Degree Self-Acting, Gas-Lubricated Bearings”, Journal of Basic Engineering, Vol. 87, pp. 199-212.

[15] Elrod, H. G., Mccabe, J. T., and Chu, T. Y., 1966, “Determination of Gas Bearing Stability by Response to a Step-Jump”, Franklin Institute Report I-A2049-27.

[16] Mori, H., and Miyamatsu, Y., 1969, “Theoretical Flow-Models for Externally Pressurized Gas Bearings”, ASME Journal of Lubrication Technology, Vol. 91, pp. 183-193.

[17] Stowell, T. B., 1971, “Pneumatic Hammer in a Gas Lubricated Externally Pressurized Annual Thrust Bearing”, ASME Journal of Lubrication Technology, Vol. 93, pp. 498-503.

[18] San Andrés, L., and Childs, D., 1997, “Angled Injection-Hydrostatic Bearings Analysis and Comparison to Test Results”, ASME Journal of Lubrication Technology, Vol. 119, pp. 179-187

[19] Lee, J. B., and Kim, K. W., 1999, “Effects of Synchronous Vibration of Bearing on Stability of Externally Pressurized Air Journal Bearings”, ASME Journal of Lubrication Technology, Vol. 121, pp. 830-835.

[20] Czolczynski, K., 1999, “Rotordynamics of Gas-Lubricated Journal Bearing System”, Springer Verlag.

[21] San Andrés and Wilde, 2001, “Finite Element Analysis of Gas Bearings for Oil-Free Turbomachinery,” Revue Européenne des Eléments Finis, Vol. 10 (6/7), pp. 769-790.

[22] Wilde, D.A., and San Andrés, L., 2003, “Comparison of Rotordynamic Analysis Predictions with the Test Response of Simple Gas Hybrid Bearings for Oil Free Turbomachinery,” ASME Paper No. GT2003-38859.

[23] Wilde, D., 2002, “Experiment Response of Gas Hybrid Bearings for High Speed Oil-Free Turbomachinery”, Mechanical Engineering M.S. Thesis, Texas A&M University, May.

[24] San Andrés, L., 2003, “XLTPGASBEAR™ Computer Program for Hydrodynamic Tilting Pad Gas Bearings & Seals,” Turbomachinery Laboratory, March.

[25] San Andrés, L., 2003, “Analysis of Performance and Rotordynamic Force Coefficients of Brush Seals with Reverse Rotation Ability,” Final Research Progress Report to Advanced Turbomachinery Solutions, Inc., March.

[26] San Andrés, L., and T. Soulas, 2002, “A Bulk Flow Model for Off-Centered Honeycomb Gas Seals,” ASME Paper 2002-GT-30286.

Appendix A
Determination of bearing (empirical) orifice discharge coefficients

Figure A.1 depicts a schematic view of the feed orifice into each bearing pad. The mass flow rate ($\dot{m}$) through an inherent orifice restrictor is given by [1]:

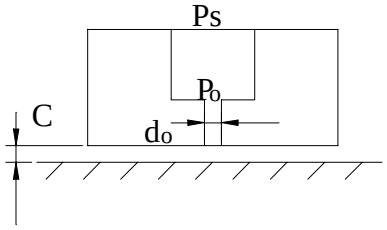

Figure A.1 Geometry of pad with feed orifice

$$\dot{m} = C_d \frac{AP_s}{(\Re T)^{1/2}} \Phi \; g \qquad \text{(A.1)}$$

where $A = \frac{\pi}{4} d_o^{\,2}$ is the orifice area, P_s is the supply pressure, P_o is the orifice pressure, and C_d is an empirical discharge coefficient. $\Re$ and T correspond to the gas constant and absolute temperature, respectively. The adiabatic coefficient $k=1.4$ for air. The pressure ratio (P_o/P_s) defines the flow function (Φ) below, and the function (g) depends on the orifice diameter (d_o) and the film clearance *(C), i.e.*

$$g = \left[1 + (\frac{d_o}{4C})^2 \right]^{-1/2} \qquad \text{(A.2)}$$

The critical pressure ratio $\frac{P_o}{P_s} = (\frac{2}{k+1})^{k/(k-1)} = 0.58$ for air. For subsonic conditions, $\frac{P_o}{P_s} > .58$, and

$$\Phi = (\frac{2k}{k-1})^{1/2} \cdot (\frac{P_o}{P_s})^{1/k} \cdot [1 - (\frac{P_o}{P_s})^{(k-1)/k}]^{1/2} \qquad \text{(A.3)}$$

while for supersonic (choked flow) conditions, $\frac{P_o}{P_s} \le 0.58$

$$\Phi = (\frac{2k}{k+1})^{1/2} \cdot (\frac{2}{k+1})^{1/(k-1)} \qquad \text{(A.4)}$$

Flow measurements are conducted to determine the orifice discharge coefficients. Flow rates are recorded with the rotor-in and out of its bearings. Table A.1 lists the constants including the orifice diameter and air properties.

Table A.1 Orifice diameter and air properties

Parameter	*Values*
Orifice diameter, d_o	0.508 mm (0.02 inch) actual or measured
Orifices per bearing	4
Air adiabatic coefficient, k	1.4
Air constant, $\mathcal{R}$	287 J/kg-K
Air temperature, T	298 K
Air density, ρ_A	1.18 kg/m^3

For the test conditions in which the rotor is out of its bearings, the orifice pressure P_o equals ambient pressure P_a. When the rotor is in place within its bearings, the orifice resistance remains the same. Thus, the condition of similar flow rates with and without rotor in place allows the determinationn of the orifice pressure and the discharge coefficient. Note that under identical flow conditions, the pressure ratio P_o/P_s must remain invariant. Table A.2 details the test flow rates without the rotor in place and the estimated orifice discharge coefficient. Table A.3 provides the same experimental information for the rotor installed within its bearings. For the estimation of the discharge coefficients (C_d), all orifices are considered identical in size. In the procedure, the number of orifices on each bearing divides the recorded mass flow rates.

Table A.2 Measured flow rates for both bearings and estimated orifice discharge coefficients. Rotor removed from bearings

Supply Pressure P_s (bar)	Pressure Ratio P_o/P_s	Measured Flow rate Kg/s ($\times 10^{-4}$)		Orifice Discharge Coefficient C_d	
		Left Bearing	Right Bearing	Left Bearing	Right Bearing
2.39	0.42	3.36	3.81	0.740	0.840
2.81	0.36	4.17	4.56	0.783	0.857
3.08	0.33	4.72	5.05	0.807	0.865
3.50	0.29	5.51	5.75	0.831	0.866
3.77	0.27	6.00	6.22	0.839	0.869
4.18	0.24	6.71	6.91	0.846	0.870
4.46	0.23	7.25	7.38	0.856	0.873
4.87	0.21	8.00	8.08	0.865	0.873
5.15	0.20	8.53	8.55	0.873	0.875
Average Orifice Discharge Coefficients				**0.827**	**0.865**

Table A.3 Measured flow rates for both bearings and estimated orifice discharge coefficients. Rotor within its bearings

Supply Pressure P_s (bar) (Left / Right)	Orifice Pressure P_o (bar) (Left/ Right)	Measured Flow rate Kg/s ($\times 10^{-4}$)		Orifice Discharge Coefficients C_d	
		Left Bearing	Right Bearing	Left Bearing	Right Bearing
2.67 / 2.81	2.09 / 2.20	0.968	1.18	0.756	0.881
3.50 / 3.63	2.48 / 2.09	1.44	1.74	0.782	0.910
4.05 / 4.32	2.62 / 1.99	1.76	2.19	0.789	0.916
4.46 / 4.74	2.65 / 1.91	1.97	2.51	0.781	0.940
4.87 / 4.74	2.68 / 1.91	2.29	2.51	0.823	0.940
5.15 / 5.15	2.63 / 1.84	2.49	2.69	0.850	0.918
Average Orifice Discharge Coefficients				**0.80**	**0.91**

Figures A.2 and A.3 depict the variation of the bearing mass flow rate versus the supply to ambient pressure ratio, for the conditions of no rotor in place and rotor within its bearings, respectively. Note that the test flow rates for each bearing are somewhat dissimilar due to poor sealing of the feed pressure chamber, which brings a not quantifiable side leakage. Note also that the actual orifice diameters in each bearing pad may not actually be identical.

Figures A.4 and A.5 show the estimated orifice discharge coefficients for the conditions of no rotor in place and rotor within its bearings, respectively. In general, the average values for the discharge coefficient noted in Tables A.2 and A.3 are adequate to provide accurate estimations of the bearing flow rate. Incidentally, note that the differences in discharge coefficient for both bearings, left and right, may stem from side leakage and uneven gas film clearances.

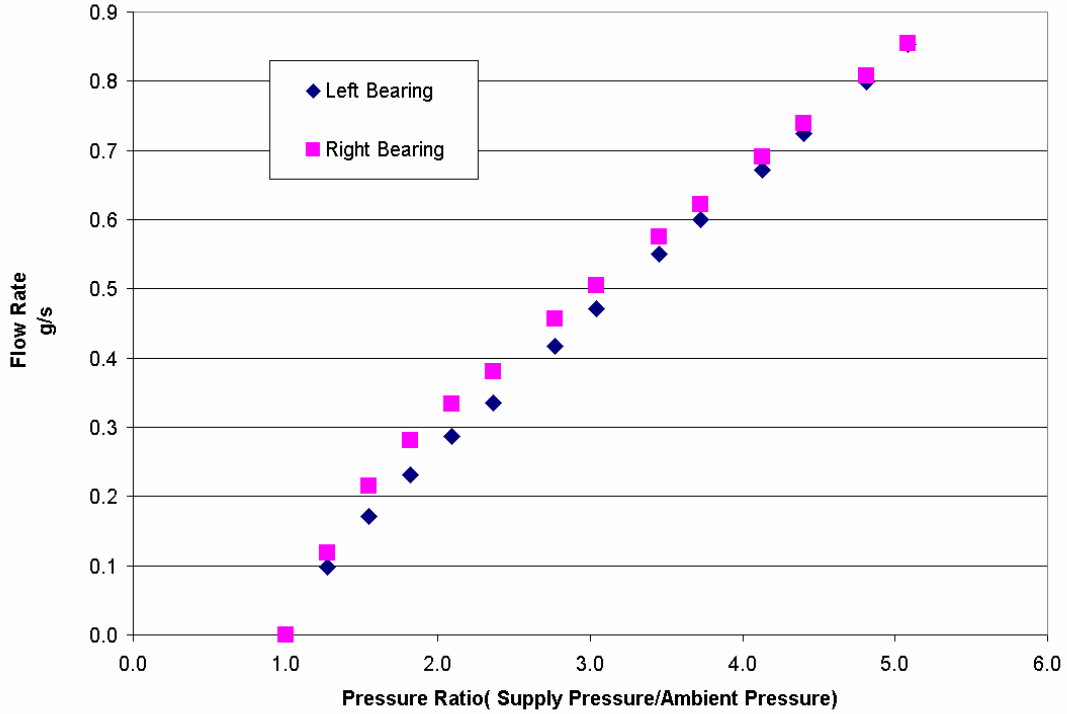

Figure A.2 Bearing mass flow rates versus supply to ambient pressure ratio. Rotor removed.

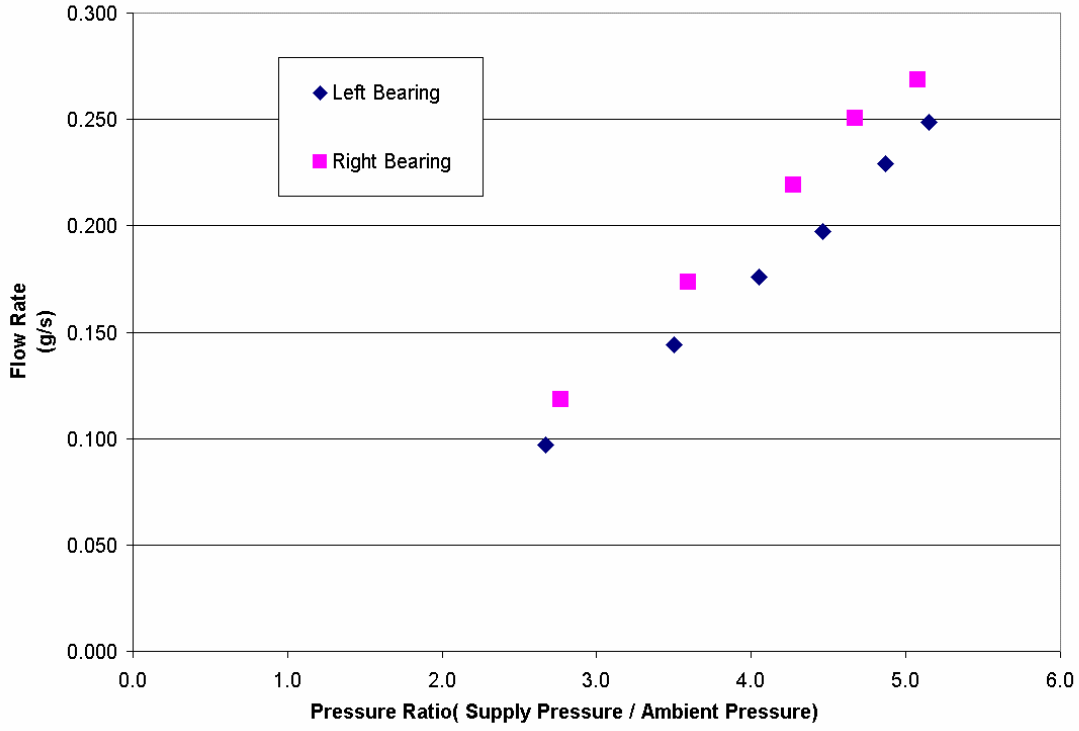

Figure A.3 Bearing mass flow rates versus supply to ambient pressure ratio. Rotor within its bearings

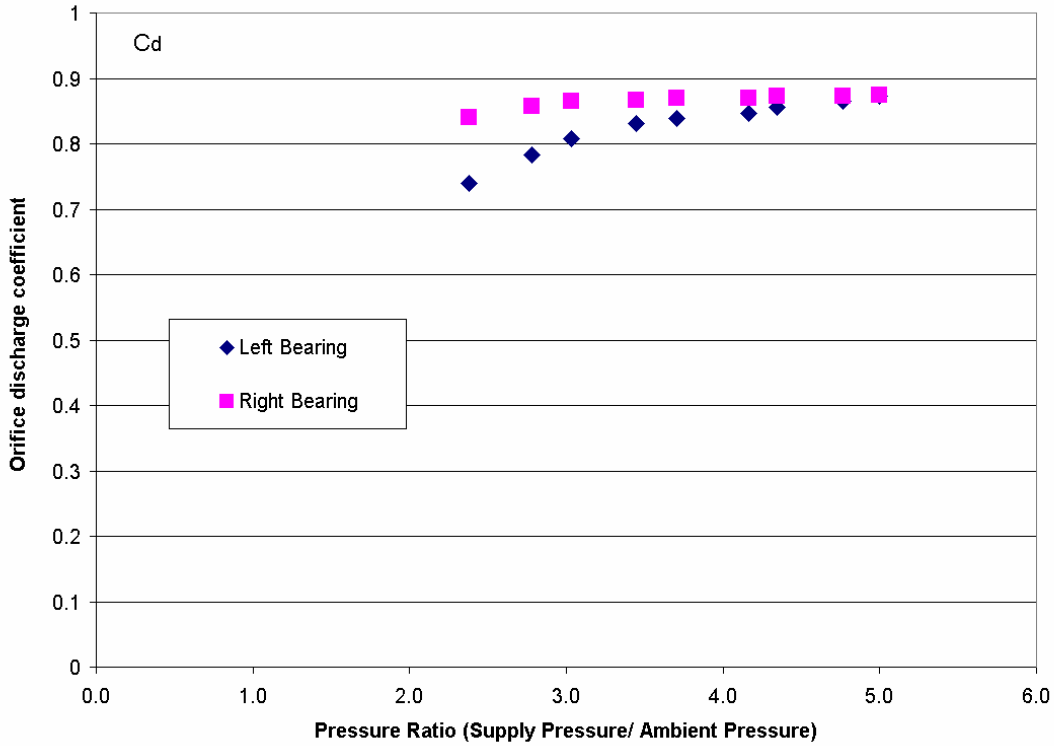

Figure A.4 Estimated orifice discharge coefficients versus supply to ambient pressure ratio. Rotor removed

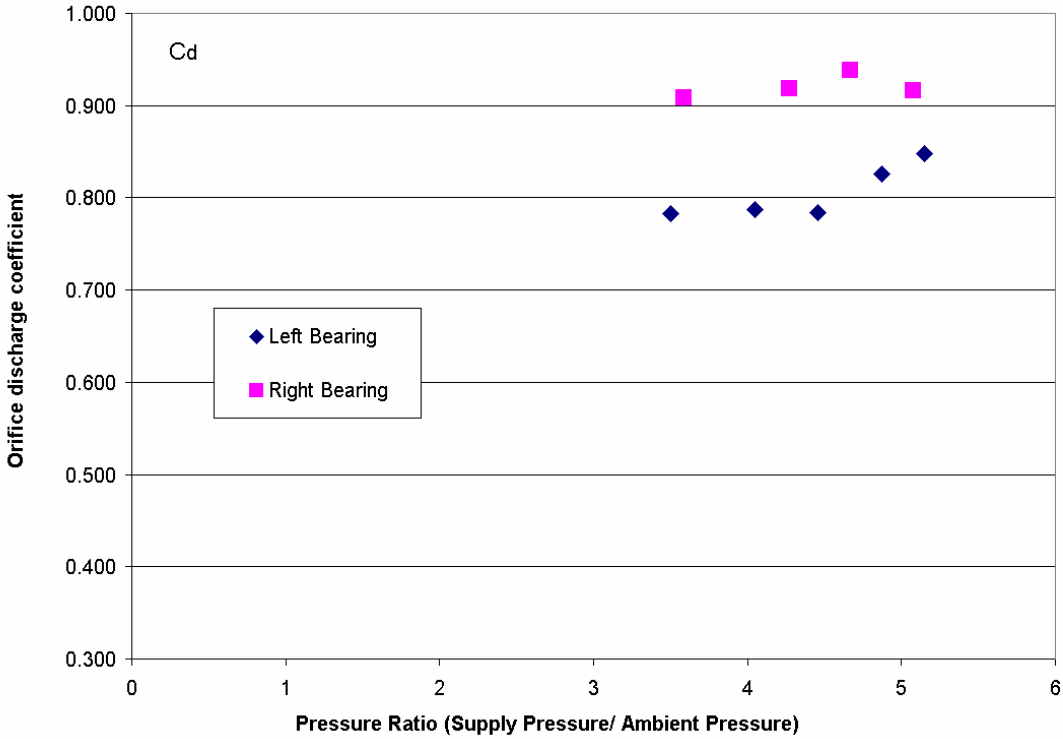

Figure A.5 Estimated orifice discharge coefficients versus supply to ambient pressure ratio. Rotor within its bearings